



UNIVERSITY OF LEEDS

This is a repository copy of *Shaping of melting and dissolving solids under natural convection*.

White Rose Research Online URL for this paper:
<http://eprints.whiterose.ac.uk/163562/>

Version: Accepted Version

Article:

Pegler, SS orcid.org/0000-0001-8373-2693 and Davies Wykes, MS (2020) Shaping of melting and dissolving solids under natural convection. *Journal of Fluid Mechanics*, 900. A35. ISSN 0022-1120

<https://doi.org/10.1017/jfm.2020.507>

© The Author(s), 2020. Published by Cambridge University Press. This article has been published in a revised form in *Journal of Fluid Mechanics* [<https://doi.org/10.1017/jfm.2020.507>]. This version is free to view and download for private research and study only. Not for re-distribution, re-sale or use in derivative works. Uploaded in accordance with the publisher's self-archiving policy.

Reuse

Items deposited in White Rose Research Online are protected by copyright, with all rights reserved unless indicated otherwise. They may be downloaded and/or printed for private study, or other acts as permitted by national copyright laws. The publisher or other rights holders may allow further reproduction and re-use of the full text version. This is indicated by the licence information on the White Rose Research Online record for the item.

Takedown

If you consider content in White Rose Research Online to be in breach of UK law, please notify us by emailing eprints@whiterose.ac.uk including the URL of the record and the reason for the withdrawal request.



eprints@whiterose.ac.uk
<https://eprints.whiterose.ac.uk/>

Shaping of melting and dissolving solids under natural convection

Samuel S. Pegler¹ and Megan S. Davies Wykes²

¹School of Mathematics, University of Leeds, Leeds, LS2 9JT, UK

²Department of Engineering, University of Cambridge, Cambridge CB2 1PZ, UK

How quickly does an ice cube melt or a lump of sugar dissolve? We address the open problem of the shapes of solids left to melt or dissolve in an ambient fluid driven by stable natural convection. The theory forms a convective form of a Stefan problem in which the evolution is controlled by a two-way coupling between the shape of the body and stable convection along its surface. A new model describing the evolution of such bodies in two-dimensional or axisymmetric geometries is developed and analysed using a combination of numerical and analytical methods. We reveal that different initial conditions lead to different evolving shapes and descent rates controlled by the interaction between the shape and flow. For the cases of initially linear surfaces (wedges or cones), the model admits similarity solutions in which the tip descends from its initial position as $t^{4/5}$. It is determined that the evolving shape always forms a parabola sufficiently near the tip which and approaches the initial shape sufficiently far below the tip. For the asymptotic limit of steeply inclined bodies, we establish a general two-tiered asymptotic structure comprising a broad $4/3$ -power intermediate near-tip region connected to a deeper parabolic region at the finest scale. The model results apply universally for any given relationship between density, viscosity, diffusivity and concentration, including two-component convection. New laboratory experiments involving the dissolution of cones of sugar candy in water are found to collapse systematically onto our theoretically predicted shapes and descent rates with no adjustable parameters.

1. Introduction

The melting and dissolution of solids plays a key role in shaping the natural world (Ristroph 2018). Examples include the melting of icebergs (e.g. Huppert & Turner 1978), the melting of glacier fronts and ice shelves (e.g. Epstein & Cheung 1983; Dutrieux *et al.* 2014; Hewitt 2020), the shaping of river beds and caves (Meakin & Jamtveit 2010), the shaping of rock spires (such as the remarkable stone forests of Madagascar), and the melting of sea ice (McPhee 2008). Everyday examples include the melting of ice cubes in air or water, the dissolution of lumps of sugar in tea and the melting of candles. While there are numerous applications and many decades of research on boundary layers formed from gravitationally stable free convection (Bejan 2013; Schlichting & Gersten 2017), a theory accounting for the interplay between shape evolution by melting or dissolution and buoyancy-driven boundary-layer dynamics has yet to be developed and explored. In all problems involving melting or dissolving boundaries in fluid flow, there is an interesting theoretical question as to what are the fundamental shapes that arise through the interplay between the fluid dynamics and the evolving boundary. Across the scope of this paper and a forthcoming paper (Pegler & Davies Wykes 2020), we will address this question, deriving a new model framework and exploring its predictions for various initial shapes. To this end, we develop a model that couples the melting or

dissolution of bodies to a flow driven by gravitationally stable free convection, solve the model equations to identify the shape evolutions, and test the model predictions in the laboratory. The analysis reveals fundamental intrinsic scales, self-similar evolutions, and regime transitions. The results ultimately provide a basis for addressing theoretically the questions of the shape assumed by bodies melting or dissolving under buoyancy.

The question of the shape assumed by a dissolving body was posed and considered experimentally by Nakouzi *et al.* (2015). In this study, the authors allowed vertical cylinders of solid glucose immersed in a water-filled tank to dissolve without an externally imposed flow. On the basis of their experimental observations, it was proposed that the tip assumes a paraboloidal shape as it descends, and that this may represent a fundamental shape for dissolving bodies under free convection. To date, no theoretical explanation for these observations, nor predictions for the descent rate and shapes of such dissolving bodies have been provided.

The analysis of stable free convection at heated, cooled or dissolving surfaces has an extensive literature for situations where the boundary remains *fixed*. The regime is characterised by a thin buoyancy-driven flow in which the driving force depends on the local slope of the underlying solid surface, whilst being generated by the thermal or solutal diffusion at the interface. Theoretical analysis of natural-convective boundary layers along fixed boundaries began with the case of fluids of constant properties and a body of uniform inclination (Ostrach 1953; Merk & Prins 1953). Subsequent studies of the underlying boundary-layer equations have in particular considered the effects of large mass-transfer rates (Acrivos 1960*a*, 1962), non-Newtonian flow (Acrivos 1960*b*), small inertia (Kuiken 1968), ambient stratification (Huppert & Turner 1980), two-component compositional convection (Josberger & Martin 1981; Carey & Gebhart 1982; Wells & Worster 2011), and reversing buoyancy (Carey *et al.* 1980). These studies essentially determine instantaneous snapshots of melt rate around a fixed shape, and neglect the evolution of shape caused by the melting or dissolution of the body. The new element we consider is to allow the boundary to evolve, with the aim to present the first theoretical predictions able to explain the general shape, asymptotic structure and descent rates of dissolving bodies immersed in a quiescent ambient. The result of the new coupling we consider is to introduce a full two-way interplay between the control of the buoyancy force by the local slope and the control of the evolution of local slope by the dissolution or melting profile of the boundary layer. The interplay is found to produce a rich problem in regard to the shapes that arise as objects melt or dissolve into their environment.

A related problem is the melting of a fully suspended sphere of wax in hot water (Mcleod *et al.* 1996). The experiments conducted in this study illustrated different melt characteristics over the overside and underside of the melting body of wax. The overside was found to develop a gravitationally stable melt film that flows over the solid body of wax. The underside was instead found to form a gravitationally unstable region of convection, producing a curtain of molten wax threads. The overside instead retains a smooth shape that melts relatively slower than the underside. By approximating both the upper and lower regions of the wax as hemispheres of different radii each with uniform melt rates, and using a thin-layer model for the melt film, the authors determine scalings for the melt rates of the upper and lower regions. The experiments illustrated a variation of the shape of the overside in melt rate with polar angle, whilst the theoretical scaling developed did not allow for evolution away from a hemisphere. For the underside, a uniform melt rate associated with the gravitationally unstable convection was proposed. Davies Wykes *et al.* (2018) have more recently considered this situation experimentally for a general variety of initial shapes resulting from dissolution of candy in water. A model of uniform and constant dissolution rate over the lower interface was shown to explain

the shape evolutions of the gravitationally unstable underside of the dissolving bodies for a variety of initial shapes. In contrast, the top half of the object dissolves more slowly and forms a smooth surface that dissolves with a spatially non-uniform distribution. We anticipate this regime to be analogous to that observed by Nakouzi *et al.* (2015). A corresponding theory to describe the evolving boundary and resulting change in shape has remained undeveloped.

The theoretical and experimental analysis of the shapes arising under dissolution, melting or erosion of bodies in fluid flow has to date considered cases of forced convection, where a body is fixed in an imposed cross-flow and buoyancy is negligible (Ristroph *et al.* 2012; Moore *et al.* 2013; Huang *et al.* 2015; Moore 2017). The experiments of Ristroph *et al.* (2012) found that an eroding sphere or vertical cylinder fixed in a maintained horizontal cross-flow form a roughly triangular self-similar shape. By coupling a potential outer flow to an inner viscous sublayer, Moore *et al.* (2013) gave a theoretical explanation of this shape as having constant shear over the front surface. A detailed examination of the shapes arising near the tip of a body allowing also for the cases of melting or dissolution was provided by Moore (2017), illustrating the development of specific power-law shapes for the tip in these various situations. For forced convection, the rate of melting, dissolution or erosion is coupled to the evolution of the surface through its effect as a boundary condition on the outer potential flow which, in turn, controls the erosion or dissolution rate through a viscous or thermal sublayer. As we will show, the problem of melting and dissolution under free convection produces a mathematically different problem that includes an inherent dependence of the driving buoyancy force on the local slope within the boundary-layer equations themselves.

We divide our study into two papers. This first paper develops our model in both two-dimensional and axisymmetric geometries, analyses the evolution of shapes resulting from a body initialised with intersecting linear surfaces (two intersecting planes in the two-dimensional case or a cone in the axisymmetric case), and presents our laboratory study of dissolving cones. The forthcoming paper (Pegler & Davies Wykes 2020) investigates more general shape evolutions and explores distinct new themes of regime transitions, the control of tip sharpening (or blunting), and the role of internal thermal conduction within melting bodies.

The present paper is divided as follows. Section 2 develops our theoretical model describing dissolving and melting bodies, discusses the underlying assumptions, and derives the form of the general tip shape. Section 3 considers the preliminary two-dimensional example in which the initial shape of the body is given by two intersecting planes. The analysis reveals similarity solutions describing the evolution of the shape in these cases and provides asymptotic solutions for the descent rate in the limits of small and steep slopes. A modified axisymmetric analogue of the model is developed and analysed in the case of initially conic bodies in section 4. Section 5 presents our laboratory study of initially conic solid candy bodies dissolving in water. We end in section 6 by discussing the limitations, generality and applicability of the results and summarising our conclusions.

2. Theoretical development

We begin by developing a general model for melting or dissolving bodies under stable natural convection. Melting and dissolving bodies can be modelled using a system of equations that are fundamentally the same, but which differ in underlying physical processes. For dissolution (e.g. candy in water), the boundary recedes in response to mass loss through molecular diffusion into the solvent. For melting (e.g. ice in water),

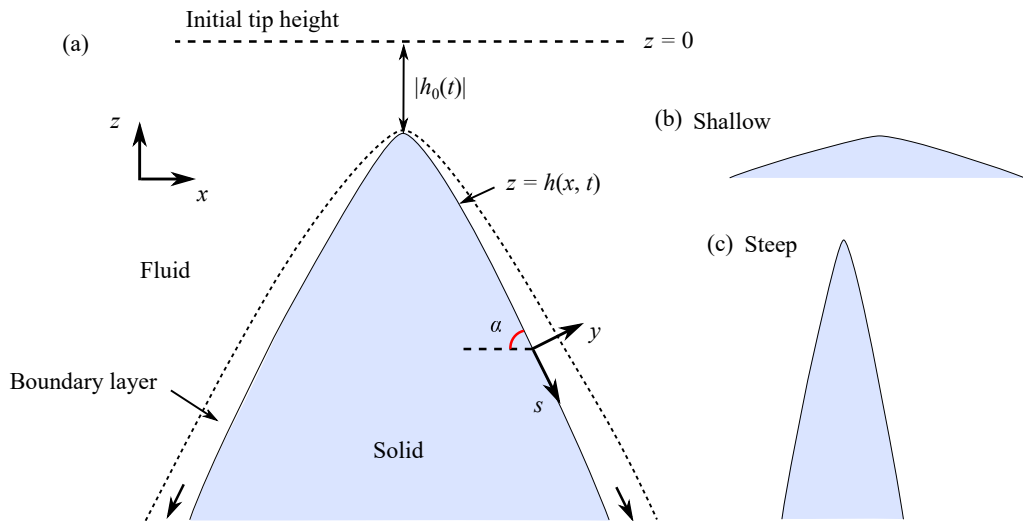


FIGURE 1. (a) Schematic illustrating the general configuration and notation for a body dissolving under gravitationally stable natural convection. Two coordinate systems are illustrated: (x, z) is fixed, while (s, y) represents a curvilinear coordinate system in which s is the arc length of the solid surface from the tip and y is the normal distance from the boundary. Panels (b) and (c) illustrate two different limits of the general model (2.16): the shallow limit, where the slope $h_x \ll 1$, and the steep limit, where $h_x \gg 1$, respectively.

the material instead undergoes a phase change induced by thermal conduction. In either case, the recession speed of the boundary is proportional to the net rate of molecular or thermal diffusion transported from or to the interface, respectively (the Stefan condition in the thermal context). In the case of a dissolving solid, diffusion is typically negligible within the interior of the solid itself, and hence the recession speed of the boundary is proportional to the flux of solute into the ambient fluid. In the context of a melting body, thermal conduction can, in principle, be important within the body. In this case, a melting body can either first equilibrate to the melt temperature, or proceed to melt with a thin conductive boundary layer under the interface; either of these cases produces an effective proportionality between exterior heat flux and recession rate (the conditions producing these distinct situations will be clarified as part of the forthcoming paper; Pegler & Davies Wykes 2020). With these caveats noted, we henceforth adopt the notation and terminology applicable for dissolving bodies.

We consider first the case of two-dimensional bodies. Let x and z denote the horizontal and vertical coordinates in the laboratory frame, respectively. Suppose that the solid has density ρ_s with surface $z = h(x, t)$ and is immersed in a quiescent, incompressible fluid of density ρ_∞ in its pure form, as illustrated in figure 1. The dissolution of the solid forms a solutal boundary layer along the exterior of the solid driven by buoyancy (natural convection). Let $\rho(x, y, t)$ denote the density of the fluid, and let $C(x, z, t)$ denote the normalised concentration of solute in the fluid, defined by

$$C(x, z, t) \equiv \frac{\rho(x, y, t) - \rho_\infty}{\rho_s - \rho_\infty}. \quad (2.1)$$

The value $C = 1$ represents pure solid ($\rho = \rho_s$) and $C = 0$ represents pure ambient fluid ($\rho = \rho_\infty$). At the interface between the solid and the fluid, we impose

$$C(x, h, t) \equiv C_i = C_{sat}, \quad (2.2)$$

where C_i is the interfacial concentration, which is assumed to equal the concentration of the solution at saturation, denoted C_{sat} . For an aqueous sucrose solution at 25 °C, the saturation concentration is $C_{sat} \approx 0.68$ (Mohos 2010). The value of C_{sat} is less than unity because solvation requires a minimum concentration of water. The saturation concentration C_{sat} depends on temperature, and thus may change if the latent heat generated by dissolution is sufficiently large (thereby requiring simultaneous solutions for both the temperature and concentration fields, rather than only the concentration). By deriving a theoretical prediction for the temperature generated by this effect (appendix A), we estimate the temperature increase to be at most ≈ 0.8 K for candy dissolving in water, resulting in a negligible change in C_{sat} of less than 0.2%. A discussion of the effect of interface temperature on interface concentration is provided in Wells & Worster (2011). Such two-component effects can in fact be incorporated directly into our model for shape evolution developed below. Nonetheless, we will neglect temperature effects for now for the purpose of simplifying our exposition.

The shape evolution is controlled by spatial and temporal variations in the rate of dissolution within the solutal boundary layer. To describe the boundary-layer flow, we use the curvilinear coordinate system (s, y) , where s is the arc length along the surface $z = h(x, t)$ measured from the tip $h_0(t) \equiv h(0, t)$, and y is the perpendicular outward distance from the surface, as shown in figure 1(a). The flux of concentration (per unit width) perpendicular to the solid boundary is, in accordance with Fick's law,

$$q(s, t) = -\kappa_i \left. \frac{\partial C}{\partial y} \right|_{y=0}, \quad (2.3)$$

where κ_i is the diffusivity of the fully saturated solution at the boundary. Let $V(s, t)$ denote the unknown speed at which the surface recedes in the direction of its normal. The speed of recession can be related to the flux (2.3) via the solute-conservation equation

$$V(s, t) = Rq(s, t) = -R\kappa_i \left. \frac{\partial C}{\partial y} \right|_{y=0}, \quad (2.4)$$

where $R \equiv \rho_i / [\rho_s(1 - C_i)]$ is a dimensionless conversion factor between concentration flux and boundary migration speed, and we have assumed here a linear relationship between mass and volume fraction. Here, we have also neglected flux in concentration in the solid interior, which could be more important in the context of melting bodies. Because the surface moves inwards, we write the vectorial form of the surface velocity as

$$\mathbf{V} = -V\mathbf{n}, \quad \text{where} \quad \mathbf{n} = \frac{\mathbf{e}_z - h_x \mathbf{e}_x}{\sqrt{1 + h_x^2}} \quad (2.5a, b)$$

is the outward normal to the surface, \mathbf{e}_x and \mathbf{e}_z are the unit vectors in the horizontal and vertical directions, and the x subscript in h_x denotes partial differentiation, $\partial h / \partial x$. Since the solid migrates with the velocity \mathbf{V} , it follows that

$$\left(\frac{\partial}{\partial t} + \mathbf{V} \cdot \nabla \right) [z - h(x, t)] = 0. \quad (2.6)$$

On simplification and use of (2.5a, b), we obtain the interface evolution equation

$$\frac{\partial h}{\partial t} = \mathbf{V} \cdot \left(\mathbf{e}_z - \mathbf{e}_x \frac{\partial h}{\partial x} \right) = -\frac{\partial s}{\partial x} V, \quad (2.7)$$

where $s_x = \sqrt{1 + h_x^2}$. Substituting (2.4) into (2.7), we obtain the evolution equation

$$\frac{\partial h}{\partial t} = -Rq \frac{\partial s}{\partial x} = R\kappa_i \frac{\partial s}{\partial x} \frac{\partial C}{\partial y} \Big|_{y=0}, \quad (2.8)$$

providing an equation for the rate of vertical descent of the solid boundary in terms of the dissolution pattern. Thus, to develop a closed model, it remains to relate the normal gradient $\partial C/\partial y$ along the surface to the shape profile $h(x, t)$.

Let u and v define the components of fluid velocity in the s (tangential) and y (normal) directions, respectively. In modelling the boundary-layer flow, we assume that the curvature of the interface is sufficiently small and that the flow is quasi-steady on the timescale of evolution of the free boundary (the criteria for these assumptions will be detailed in section 2.3). The equations describing steady free-convective laminar boundary layers read (Ostrach 1953)

$$\frac{\partial u}{\partial s} + \frac{\partial v}{\partial y} = 0, \quad (2.9)$$

$$\rho \left(u \frac{\partial u}{\partial s} + v \frac{\partial u}{\partial y} \right) = \frac{\partial}{\partial y} \left(\mu \frac{\partial u}{\partial y} \right) + \Delta \rho_s g \sin[\alpha(s, t)] C, \quad (2.10)$$

$$u \frac{\partial C}{\partial s} + v \frac{\partial C}{\partial y} = \frac{\partial}{\partial y} \left(\kappa \frac{\partial C}{\partial y} \right), \quad (2.11)$$

where $\alpha(s, t)$ is the angle of the slope to the horizontal (the angle α is shown red in figure 1), and $\Delta \rho_s \equiv \rho_s - \rho_\infty$. Equations (2.9)–(2.11) represent the conservation of total fluid mass, momentum and solute mass, respectively.

We allow here for general dependences of viscosity $\mu(C)$, diffusivity $\kappa(C)$ and density $\rho(C)$ on the concentration C . For many fluids, including rock candy dissolving in water, the viscosity of the solution $\mu(C)$ can vary by many orders of magnitude (for a solution of rock candy, μ will vary by at least two orders of magnitude; Quintas *et al.* 2006). Since viscosity and molecular diffusion are related approximately inversely in accordance with the Stokes-Einstein relation, $\kappa \propto \mu^{-1}$ (e.g. Mohos 2010; Price *et al.* 2016), order-of-magnitude variations in molecular diffusivity $\kappa(C)$ will also apply. Fortunately, these complications can all be encapsulated concisely within a single parameter.

The boundary-layer system (2.9)–(2.11) is fifth order and hence requires five boundary conditions. One is provided by the Dirichlet condition on the interface concentration (2.2). Further conditions are provided by the no-slip condition and normal-velocity condition at the migrating solid boundary given by

$$u = 0, \quad v = (\rho_s/\rho_i)V, \quad \text{on } y = 0, \quad (2.12a,b)$$

respectively (e.g. Wells & Worster 2011). The normal velocity condition (2.12b) represents the sum of two contributions: $([(\rho_s - \rho_i)/\rho_i]V + V) = (\rho_s/\rho_i)V$. The first is the speed accounting for the net sourcing of fluid caused by the density difference between the solid and the adjacent solution. The second contribution accounts for the fact that $y = 0$ is moving inwards at velocity V , and thus V must be added to account for this frame change. Finally, we impose

$$C \rightarrow 0, \quad u \rightarrow 0 \quad \text{as } y \rightarrow \infty, \quad (2.13a,b)$$

completing the set of conditions needed to close the boundary-layer system.

For any given surface profile $h(x, t)$, the system (2.9)–(2.13) forms a parabolic boundary-value problem for $C(s, y, t)$. Once C is known, the normal gradient $\partial C/\partial y$ on $y = 0$ can be evaluated and the surface descent rate $\partial h/\partial t$ determined using (2.8). The surface can then be evolved in time and the process repeated. The coupled model (2.8)–(2.13) generalises models of natural convection along dissolving or melting boundaries (Schlichting & Gersten 2017) to incorporate the two-way coupling between boundary-layer dynamics and the evolution of the boundary. Conversely, the model forms a variation of classical (purely diffusive) Stefan problems in which the migration of a melting or solidifying boundary is modelled using conductive transport processes (Stefan 1891; Jaeger & Carslaw 1959) to assume instead that the shape evolution is driven by the buoyancy-driven convection along the exterior of the body.

2.1. Analytical reduction for large Schmidt number

For general situations in which all terms in the momentum equation (2.10) contribute, one could consider the boundary-layer system (2.9)–(2.13) alongside (2.8). However, we note that if the Schmidt number $Sc \equiv \mu/\rho\kappa$ is sufficiently large, a major simplification of the boundary-layer system (2.9)–(2.13) is available that allows a single integro-differential hyperbolic equation describing the evolution of $h(x, t)$ to be developed. We consider this situation first as an inroad for clearly demonstrating many of the simplified scalings, properties and self-similar forms underlying dissolving shapes. The effects of reinstating inertia are discussed in section 6.

Convective boundary-layers described by (2.9)–(2.13) will generally involve both a viscous sublayer, in which viscous stresses become important, and a diffusive sublayer in which the transfer of solute is localised. The relative size of the viscous sublayer compared to the solutal layer is characterised by the Schmidt number $Sc \equiv \nu/\kappa$. If $Sc \gg 1$, the viscous sublayer is considerably larger than the solutal layer, such that the solutal layer forms an inner sublayer inside the viscous sublayer. Exterior to the viscous sublayer lies an inertial outer region in which the transition to the far-field stagnancy condition (2.13) occurs. More specifically, for the purpose of determining the solutal flux along the boundary, it is sufficient to consider just the viscous sublayer subject to a matching condition of zero stress on its far-field, a system we review in appendix C. As shown by Kuiken (1968), the neglect of inertia in the solutal region introduces an error of less than 20% in the predicted flux for all $Sc > 1$, implying that even order-unity values of Sc are well approximated by the $Sc \rightarrow \infty$ limit. Since the Schmidt number is comprised purely of material parameters, and is independent of the shape of the body, for example, it is straightforward to evaluate for a given configuration. For example, $Sc \approx 2 \times 10^3$ (dilute) to 8×10^6 (saturated) using the kinematic viscosity and diffusivity for dilute and saturated solutions of sucrose in water, respectively, and hence $Sc \gg 1$ is firmly satisfied in this context.

The analytical reduction that arises for $Sc \rightarrow \infty$ is based on a transformation of the boundary-layer subsystem describing the viscous sublayer that eliminates the interface slope (Acrivos 1960*a*), leaving a transformed boundary-layer subsystem that is independent of the surface profile (the transformed system is equivalent to the similarity system describing free convection along a vertical wall, for example). By considering the similarity solution to the transformed system and then recasting the system back in terms of the original variables, one obtains the dissolution profile along an arbitrary

two-dimensional shape as

$$q(s, t) = -\kappa_i \left. \frac{\partial C}{\partial y} \right|_{y=0} = \frac{D \sin[\alpha(s, t)]^{1/3}}{\left(\int_0^s \sin[\alpha(s, t)]^{1/3} ds \right)^{1/4}}, \quad (2.14)$$

where $D \equiv \gamma \kappa_i C_i (\Delta \rho_s g C_i / \kappa_\infty \mu_\infty)^{1/4}$ is a constant material parameter, μ_∞ and κ_∞ are the viscosity and diffusivity of the solvent, and γ is a dimensionless number. The result above is derived by Acrivos (1960a), and a step-by-step review of the derivation is provided in appendix C. As discussed in the appendix, the dimensionless prefactor γ depends on the material properties of the fluid and solid under consideration, including any dependences of μ , κ and ρ on the concentration C , as any two-component temperature effects. The presence of $\sin \alpha$ in the numerator of (2.14) implies that a larger along-slope component of buoyancy drives faster convective transport locally and hence more efficient dissolution. The integral in the denominator is a ‘memory term’ representing the total dissolution between the tip and the position s . The increase of this integral with s represents the insulating effect of solute accumulation, which reduces the dissolution rate as the boundary layer grows downstream.

Using (2.14), the recession rate of the boundary can be determined as

$$V(s, t) = Rq = \frac{A \sin[\alpha(s, t)]^{1/3}}{\left(\int_0^s \sin[\alpha(s, t)]^{1/3} ds \right)^{1/4}}, \quad (2.15)$$

where $A \equiv RD \equiv \gamma R \kappa_i C_i (\Delta \rho_s g C_i / \kappa_\infty \mu_\infty)^{1/4}$. The parameter A represents all effects on dissolution associated with the material properties of the fluid and the solid, and is referred to herein as the *convective strength*. This is distinct from the effects of shape, which are controlled by the terms in expression (2.15) depending on $\alpha(s, t)$. In particular, the number A encapsulates, via γ , the full functional dependences of viscosity μ , diffusivity κ and density ρ on the concentration C . The parameter A could, in principle, be determined by measuring the functions of $\mu(C)$, $\kappa(C)$ and $\rho(C)$ for the fluid of interest and solving the similarity system (C5)–(C6) for γ and, in turn, A . Alternatively, one could measure A empirically for a given system of interest using a ‘one off’ observation of an instantaneous recession rate, circumventing the need to measure $\mu(C)$, $\kappa(C)$ and $\rho(C)$ explicitly and solving (C5)–(C6). This direct empirical method of inferring A will be discussed further in section 5. For a vertical wall (for which $\alpha = \pi/2$ and $s = -z$), (2.15) reduces to $V = A(-z)^{-1/4}$, giving the $(-z)^{-1/4}$ dissolution profile along a wall of constant inclination (e.g. Ostrach 1953). The convective strength A can thus be interpreted as the prefactor to $(-z)^{-1/4}$ that would apply in an expression for the instantaneous recession speed along a vertical wall for the fluid-solid configuration under consideration. In this case, the recession speed at the top of the vertical wall ($z = 0$) is, at least instantaneously, infinite. However, once the evolution of the boundary is also incorporated into the model (see below), the shape at $z = 0$ would be instantaneously smoothed in such a way as to produce a finite recession speed for all subsequent times.

Using (2.15), we couple the recession speed $V(s, t)$ fully to the profile $h(x, t)$ via (2.7). Substituting (2.15) into the solute conservation equation (2.7) and noting that $\sin \alpha = h_x/s_x$ and $ds = s_x dx$, we obtain the shape evolution equation

$$h_t = \frac{-A |h_x s_x^2|^{1/3}}{\left(\int_0^x |h_x s_x^2|^{1/3} dx \right)^{1/4}}, \quad s_x = \sqrt{1 + h_x^2}. \quad (2.16)$$

This result yields an independent partial integro-differential equation describing the

evolution of the dissolving solid interface $h(x, t)$. The equation shows that the evolution of a dissolving or melting boundary in free convection is governed by a hyperbolic system relating the descent rate h_t to the slope h_x . The numerator represents a dependence of the descent rate on the *local* value of the slope h_x , showing that the dissolution rate increases with the local slope. The integral in the denominator represents a *global* dependence of the descent rate at a position x on all the values of h_x between the tip and the position x . This contribution represents the insulating effect of concentration accumulation between the tip and the position x .

2.2. Tip shape and its relation to instantaneous descent rate

Before solving (2.16), we first note several implied properties of the local tip shape and its relationship to the instantaneous rate of tip descent. To seek the admissible tip shapes, we try a power-law $h \propto x^a$, where $a > 1$ is a constant, in (2.16) and take the near-tip limit $x \rightarrow 0$. We find that (2.16) then simplifies to

$$h_t \propto x^{(a-2)/4} \quad (x \rightarrow 0). \quad (2.17)$$

The rate of tip descent h_t is therefore finite if and only if the tip is parabolic, $a = 2$. Otherwise, the tip would move infinitely quickly ($a < 2$) or remain stationary ($a > 2$). The tip will therefore assume a parabola as it descends at a finite, non-zero speed. This provides a theoretical answer to the question posed by Nakouzi *et al.* (2015) on whether the shapes of buoyancy-driven descending tips converge to a universal shape, and explains the emergence of a paraboloidal shape indicated by their experimental observations. It should be noted, however, that the parabola only applies close to the tip. The precise asymptotic meaning of how close, and an identification of the different shapes that arise exterior to the parabolic region, will be determined in our later analyses. Indeed, the parabolic region can be so small in the case of steep bodies that an entirely different near-tip shape is more representative. Previous theoretical work on forced convection has found that the local shape of a tip dissolving, melting or eroding in a fluid flow is that which produces a boundary layer with a locally smooth recession rate (Ristroph *et al.* 2012; Moore *et al.* 2013; Huang *et al.* 2015; Moore 2017). We note that the parabola is the unique shape that satisfies the property of a locally uniform recession rate under stable natural convection in the limit $h_x \rightarrow 0$ (this property is shown by the expression for q in (C 9) given in appendix C).

The implied parabolic profile near the tip can be written

$$h \sim h_0(t) - \frac{1}{2}S(t)x^2 \quad (x \rightarrow 0), \quad (2.18)$$

where $S(t) = |h_{xx}(0, t)|$ is the tip curvature or *sharpness*. Substituting the implied slope $h_x = -S(t)x$ into (2.16), we determine the general law relating tip speed to tip sharpness,

$$\frac{dh_0}{dt} = -A \left(\frac{4}{3}S(t) \right)^{1/4}. \quad (2.19)$$

Sharper tips thus descend faster, at a rate directly proportional to the convective strength A and the 1/4-power of the tip curvature $S(t)$.

2.3. Assumptions underlying the boundary-layer model

A foundational assumption of the boundary-layer model of (2.9)–(2.11) is that the curvature of the interface is sufficiently small and the boundary-layer sufficiently thin that $\delta h_{ss} \ll 1$, where δ is the boundary layer thickness. In this limit, the derivatives with respect to y , i.e. the normal shear stress and normal diffusion, yield the dominant

contributions to the diffusive and viscous-stress terms, as assumed in (2.10) and (2.11). This approximation is strongly satisfied in our laboratory experiments, for example, where the boundary layer thickness in the laminar regime is small enough to not be visible (figure 14) and is estimated to be less than 1 mm. A further underlying assumption is that the boundary-layer remains laminar and attached to the surface. This aspect will be discussed further in section 6.

The system (2.9)–(2.11) is underlain by two further assumptions relating to assumed quasi-steadiness of the flow and the form of the buoyancy force. The first of these arises from the neglect of the time derivatives in (2.10) and (2.11) on the basis that the speed of recession of the surface is much slower than the adjustment time scale of the boundary layer. As an example, the typical speed of the interface in our experiments is ~ 1 cm hour $^{-1}$, while the boundary-layer flow rate is ~ 1 cm s $^{-1}$, indicating that quasi-steadiness is strongly satisfied. To provide an explicit non-dimensional index to assess the satisfaction of quasi-steadiness and the relative importance of ambient convection during the dissolution of the body, we define a dimensionless number

$$\Gamma \equiv V/u, \quad (2.20)$$

representing the ratio of the recession speed to the rate of convective transport. If $\Gamma \ll 1$ across the majority of the shape, the boundary layer will adjust effectively instantaneously to the solution of the steady boundary-layer equations (2.9)–(2.11). If instead $\Gamma = O(1)$, the boundary-layer flow will evolve on the same time scale as the interface. In this case, a generalisation of the boundary-layer equations (2.9)–(2.11) to include time dependence could be considered. If $\Gamma \gg 1$, the interface will recede considerably faster than the boundary-layer flow. In this limit, convection is negligible and the melt rate is controlled by time-dependent diffusion in the manner of a classical (purely diffusive) Stefan problem. Values of $\Gamma \ll 1$ apply for sufficiently large bodies. To show this, we consider the value of Γ for two illustrative examples. For these estimates, we use the scalings for the boundary-layer velocity u given in section C.1. For the case of a parabolic shape, (2.19) yields the scaling $V \sim AS^{1/4}$ and (C 9) yields $u \sim \kappa_\infty(SG_*)^{1/2}x$, where $G_* = \Delta\rho_s g C_i / \kappa_\infty \mu_\infty$. Substituting these expressions into (2.20), we obtain $\Gamma \sim l_1/x$, where $l_1 \equiv (R^4/S G_*)^{1/4}$ is an intrinsic length scale. Thus, there is a location l_1 such that the recession speed is faster than the flow for $x \lesssim l_1$ and the recession speed is slower than the flow for $x \gtrsim l_1$. Therefore, if $l/l_1 \gg 1$ where l is the horizontal length scale of the body, the shape evolution is predominantly controlled by the quasi-steady equations. Our laboratory experiments presented in section 5 form a steep body with approximately linear surfaces. To evaluate Γ for this case, we note that (2.15) yields the scaling $V \sim A|z|^{-1/4}$ and (C 10) yields $u \sim \kappa_\infty(G_*|z|)^{1/2}$, such that $\Gamma \sim (l_2/|z|)^{3/4}$, where $l_2 \equiv (R^4/G_*)^{1/3} = (A^2/\kappa_i^2 G_*)^{2/3}$ is a length scale. This scale is < 1 μm for our experiments, indicating that quasi-steadiness is strongly satisfied throughout the majority of the flow.

The form of the buoyancy term on the right-hand side of (2.10) is standard in the modelling of free convection along vertical and inclined walls (Schlichting & Gersten 2017). However, we wish to allow for shallow slopes, $h_x \ll 1$, for which the buoyancy force can also be affected by horizontal gradients in hydrostatic pressure caused by the stratified density field (Stewartson 1958). By considering a scaling analysis of a generalised system of boundary-layer equations detailed in appendix B, we discuss the transition of the flow from a *gradient-driven* region near the tip, in which gradients in hydrostatic pressure contribute to driving the flow, to a *slope-driven* region wherein these gradients are negligible and the flow is driven dominantly by the along-slope component of buoyancy, as assumed in (2.10). Assuming a surface boundary of the general power-law

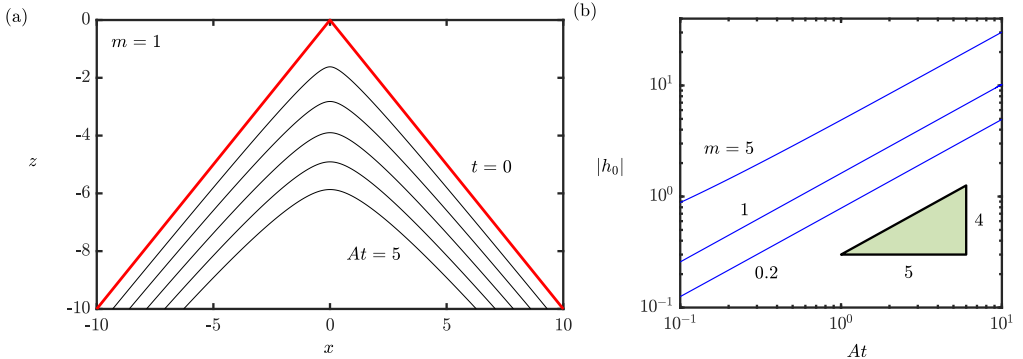


FIGURE 2. Numerical solutions to the full model (2.16) subject to the initial condition (3.1). Panel (a) shows the evolution for the case in which the shape is initialised as two intersecting planes of slope $m = 1$. The progression is shown at (scaled) times of $At = 0, 1, \dots, 5$, illustrating the rounding of the tip. The initial shape is shown red. Panel (b) shows tip displacement with time for $m = 0.2, 1$ and 5 , demonstrating the power-law $|h_0| \sim (At)^{4/5}$ implied by the similarity scaling of (3.2).

form $h \sim -c_n x^n$, where c_n and n are constants, the transition between the gradient and slope driven regimes is determined to occur over the length scale

$$\mathcal{L} \equiv (\mathcal{L}_*^3 c_n^{-5})^{\frac{1}{5n-2}}, \quad \text{where} \quad \mathcal{L}_* \equiv \left(\frac{\mu\kappa}{\Delta\rho_s g} \right)^{1/3}. \quad (2.21)$$

The case $n = 1$ of the above was derived by Stewartson (1958), who also discussed its interpretation as the scale on which a gradient-driven region applies for $x \ll \mathcal{L}$. Assuming a representative linear surface, $c_1 = m$, we estimate that $\mathcal{L} = (2 \times 10^{-5} m^{-5/3})$ metres using values representative of our laboratory experiments. The length is $\approx 1 \mu\text{m}$ for our shallowest laboratory experiment ($m \approx 5.8$). The gradient-driven region is therefore indicated to lie very close to the tip. In order for the gradient-driven region to be appreciable at the laboratory scale (taking $\mathcal{L} = 1 \text{ cm}$ for instance), the slope must be $m \lesssim 2 \times 10^{-3}$. The gradient-driven regime (Stewartson 1958; Neufeld *et al.* 2010) therefore applies only briefly, even for a shallow slope. On this basis, we anticipate that the along-slope form of buoyancy represented by the model of (2.10) is likely to represent the most widely applicable regime describing dissolving and melting bodies for appreciable shape changes at the laboratory scale and larger.

3. Mathematical analysis

Equation (2.16) describes the evolution of dissolving two-dimensional bodies, subject to specification of any given initial shape $h(x, 0)$ with a single maximum. Across the scope of this paper and the companion, we will allow for general initial shapes of the form $h(x, 0) \propto -|x|^n$, where $n > 0$. This form encompasses initially rectangular cross-sectioned surfaces ($n = \infty$), smooth parabolas ($n = 2$), wedges ($n = 1$), and sharp concave surfaces (e.g. $n = 1/2$). General values of n will be found to exhibit a variety of asymptotic transitions between different regimes, owing to the existence of an explicit time scale in the problem $t \sim AL^{5/4}$ representing the time scale for the tip to descend a distance comparable to the initial size of the body L (Pegler & Davies Wykes 2020). In the unique case $n = 1$, no such time-independent length scale exists (to be shown in section 3.1 below), resulting in similarity solutions that apply for all time. As a stepping

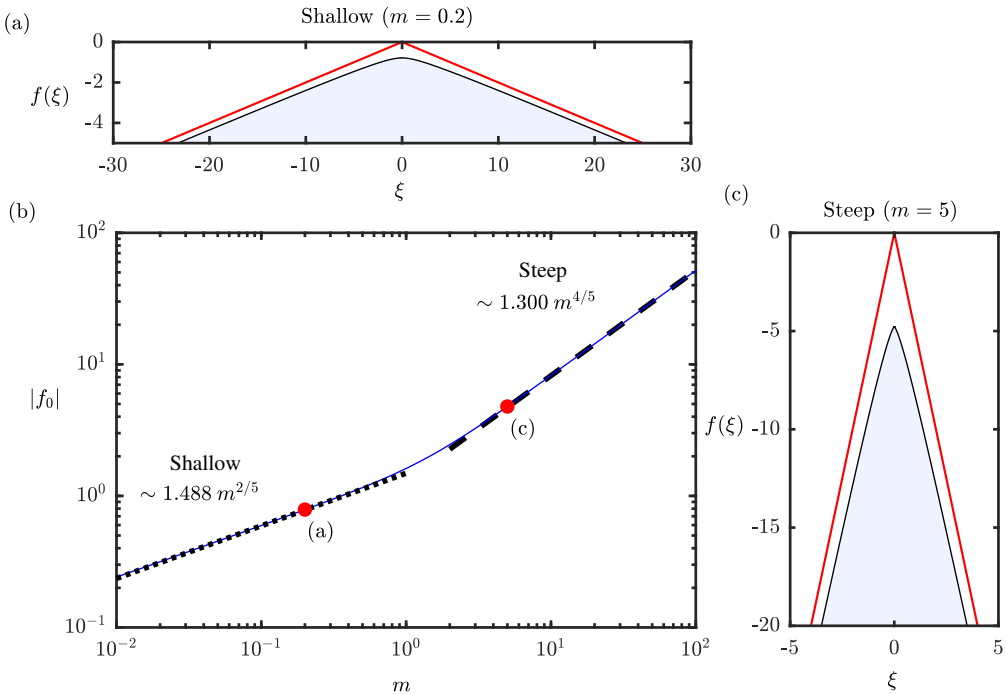


FIGURE 3. Similarity solutions describing the shape evolution of a body initially comprised of two intersecting planes, determined by numerically solving the ordinary integro-differential system (3.4). Panels (a) and (c) show the solutions for the shallow case $m = 0.2$ and the steep case $m = 5$, respectively. Panel (b) shows the universal relationship between tip-descent prefactor $|f_0|$ which controls the rate of descent of the tip in accordance with (3.5). The asymptotes in the limits of $m \rightarrow 0$ and $m \rightarrow \infty$ are shown as a black dotted line and a black dashed line, respectively, as predicted by the reduced asymptotic models derived in section 4. The locations of the examples in (a) and (c) are indicated by red circles.

stone, we begin here by analysing these similarity solutions, reserving a consideration of general n for the forthcoming paper. Thus, we specify the initial condition

$$h(x, 0) = -m|x|, \quad (3.1)$$

where m is the initial magnitude of the slopes of the two adjoining planes, forming the unique dimensionless parameter in the problem.

As a preliminary illustration of the model solutions, we present a selection of direct numerical solutions of (2.16) subject to (3.1). For this, we applied the second-order upwind finite-difference scheme detailed in appendix D. A typical progression is shown in figure 2 for the case $m = 1$ for increasing times of $(At) = 1, 2, \dots, 5$, where the initial shape is shown red. The solution illustrates the progressive rounding of the tip with time superposed with an approximately uniform global recession rate. The evolution of the tip $h_0(t) \equiv h(0, t)$ is shown for $m = 0.2, 1$ and 5 in figure 2(b). In each case, the tip descends in proportion to $t^{4/5}$ for all time with a prefactor that increases with steepness m . The steeper case dissolves faster because the larger along-slope component of buoyancy drives a faster boundary-layer flow. The persistent $|h_0| \propto t^{4/5}$ power law indicates the existence of self-similar evolutions arising for every value of the initial slope m .

3.1. Similarity solutions

We begin by attempting to construct an intrinsic length scale from the two equations (2.16) and (3.1) using scaling analysis. Depending on whether this length scale must incorporate time t explicitly, one can assess whether the system is likely to support self-similar solutions. The initial condition (3.1) yields the direct scaling between horizontal and vertical length scales, $h \sim x$. The governing equation (2.16) yields the further scaling relationship

$$x \sim h \sim (At)^{4/5}, \quad (3.2a,b)$$

indicating that the evolution of the body remains invariant on scaling both the vertical and horizontal dimensions by a factor of $(At)^{4/5}$. With all the scaling relationships in the system now applied, we deduce that no intrinsic time-independent length scale can be constructed. Thus, the system is anticipated to support self-similar evolutions. Since the system depends on the dimensionless number m in (3.1), different similarity solutions can be anticipated to arise for each value of m . To explore these solutions, let us recast the system in terms of the similarity variables motivated by (3.2), namely,

$$x = (At)^{4/5}\xi, \quad h(x, t) = (At)^{4/5}f(\xi), \quad (3.3)$$

where ξ is the similarity coordinate and $f(\xi)$ is the shape function. The governing equation (2.16) and initial condition (3.1) transform to

$$\frac{4}{5}(f - \xi f') = \frac{-|f' s'^2|^{1/3}}{\left(\int_0^\xi |f' s'^2|^{1/3} d\xi\right)^{1/4}}, \quad f(\infty) \sim -m\xi, \quad (3.4a,b)$$

respectively, where $s' = \sqrt{1 + (f')^2}$. The large- ξ asymptotic condition (3.4) arises from the initial condition (3.1) because the limit $t \rightarrow 0$ corresponds to the limit $\xi = (At)^{-4/5}x \rightarrow \infty$ for all $x > 0$. Physically, this condition applies because the dissolution rate tends to zero as the boundary layer thickness grows with x . Hence, the shape asymptotes to its initial shape in the limit $x \rightarrow \infty$. The similarity system above forms an ordinary integro-differential system for $f(\xi)$, giving a different solution for each value of m .

We solved (3.4a, b) numerically using a shooting method. For a given value of m , we begin by choosing a trial value of the unknown tip height, $f_0 \equiv f(0)$. We then integrate (3.4a) forwards from this trial value to a large value of ξ , denoted ξ_∞ . The integration was conducted using a Runge-Kutta integrator. Since (3.4a) cannot be expressed explicitly in terms of f' , we employed the implicit Matlab integrator `ode15i`. The numerically predicted value of the gradient $f'(\xi)$ was then compared with the far-field value $-m$ required by (3.4b). Depending on whether the value was greater than or less m , a new trial value of f_0 was formulated. The bisection method was applied until the error $|f'(\xi_\infty) + m| < 10^{-6}$, for typical values of the integration length taken as $\xi_\infty > 10^3 m^{-1}$.

Our resulting numerical solutions are shown in figure 3. Panels (a) and (c) illustrate the similarity solution arising for the shallow slope $m = 0.2$ and the steep slope $m = 5$, respectively. The initial shapes are shown as red curves. The self-similar shapes exhibit rounded tips, with the steeper case retaining a relatively sharper tip that descends faster. In accordance with the similarity scaling of (3.3), the tip descends according to

$$h_0(t) = f_0(At)^{4/5}, \quad (3.5)$$

where $f_0 \equiv f(0)$ is the *tip-descent prefactor*. The plot of the tip-descent prefactor $|f_0|$ is shown as a function of m in figure 3. The prefactor $|f_0|$ increases with m , consistent with

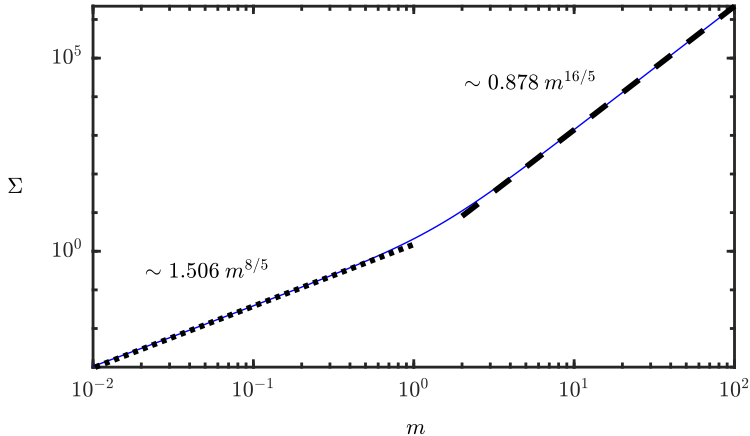


FIGURE 4. The tip-sharpness prefactor Σ defined by (3.6) as a function of the initial slope m , determined using (3.7). The shallow and steep asymptotic predictions of (3.13) and (3.20b) are shown by the dotted and dashed black lines, respectively.

steeper shapes receding faster. The power-exponent of f_0 switches from $2/5$ for small m to $4/5$ for large m , indicating the existence of distinct asymptotic regimes arising for shallow and steep dissolving bodies.

Before considering these limiting regimes, we consider the tip sharpness predicted by the self-similar evolutions. In terms of (3.3), the tip sharpness is

$$S(t) = |h_{xx}| = \Sigma (At)^{-4/5}, \quad (3.6)$$

where $\Sigma \equiv |f''(0)|$, implying that the surfaces blunt progressively as $t^{-4/5}$. This is consistent with the blunting exhibited by our numerical solution in figure 2. Surprisingly, dissolving shapes do not always blunt with time, a result that will be demonstrated in the companion paper (Pegler & Davies Wykes 2020). It will be shown in particular that the tips of more general shapes (e.g. initially rectangular or cylindrical objects) instead sharpen progressively.

Recasting (2.19) in similarity form, we obtain

$$\Sigma = \frac{3}{4} \left(\frac{4}{5} f_0 \right)^4, \quad (3.7)$$

which allows us to evaluate Σ automatically in terms of the already determined f_0 . As shown in figure 4, the sharpness prefactor increases with m , implying that initially steeper shapes retain sharper tips. It should be noted that slope and sharpness need not always increase together, as will be demonstrated in the forthcoming paper.

3.2. The shallow limit

If the slope is small, $h_x \ll 1$, then the along-slope component of gravity is given to leading-order directly by the slope of the surface, $\sin \alpha \approx -h_x$. Under this approximation, the governing equation (2.16) simplifies to

$$\frac{\partial h}{\partial t} \approx \frac{-A|h_x|^{1/3}}{\left(\int_0^x |h_x|^{1/3} dx \right)^{1/4}}, \quad (3.8)$$

producing a simplified shallow version of the general theory. In this limit, the similarity

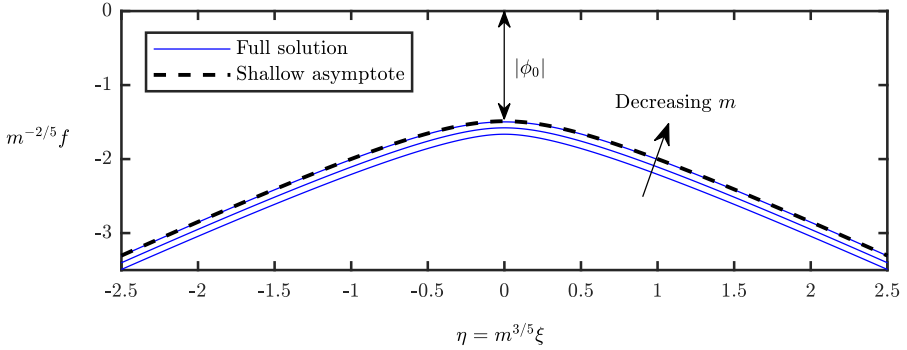


FIGURE 5. The universal limiting similarity solution arising for shallow slope ($m \rightarrow 0$), obtained by solving (3.11a, b) numerically (dashed black curve) plotted in terms of the rescaled coordinates (3.10). Numerical solutions to the full similarity system (3.4a, b) (blue curves) are shown for $m = 1.2, 0.8$ and 0.2 , illustrating convergence to the shallow theory as $m \rightarrow 0$.

system (2.19a, b) reduces to

$$\frac{4}{5}(f - \xi f') = \frac{-|f'|^{1/3}}{\left(\int_0^\xi |f'|^{1/3} d\xi\right)^{1/4}}, \quad f(\infty) \sim -m\xi. \quad (3.9a, b)$$

With the approximation of shallowness applied, it is now possible to eliminate the initial slope m from the system. To do this, we recast the reduced system above in terms of the scaled variables

$$\eta = m^{3/5}\xi, \quad \phi = m^{-2/5}f, \quad (3.10)$$

equations (3.9a, b) become

$$\frac{4}{5}(\phi - \eta\phi') = \frac{-|\phi'|^{1/3}}{\left(\int_0^\eta |\phi'|^{1/3} d\eta\right)^{1/4}}, \quad \phi(\infty) \sim -\eta, \quad (3.11a, b)$$

which has rendered the system free of the only parameter m . The solution to this reduced system thus yields a universal similarity solution describing the shape of dissolving shallow bodies. The solution, determined using the same numerical scheme as that used for the full model, is shown as a dashed black curve in figure 5 alongside a selection of solutions to the full model (3.4) with decreasing m , illustrating the approach of the full solutions towards the shallow regime as $m \rightarrow 0$. The (scaled) tip prefactor determined from the numerical solution is $\phi_0 \approx -1.49$. Using (3.10), we determine the tip-descent prefactor as

$$|f_0| \sim 1.49 m^{2/5}. \quad (3.12)$$

This result is shown as a dotted black line in figure 3, where it is confirmed to describe the tip-descent prefactor as $m \rightarrow 0$.

Substituting (3.12) into (3.6), we obtain the prediction for the sharpness prefactor

$$\Sigma = 1.50 m^{8/5}. \quad (3.13)$$

The sharpness of tips formed by dissolving shallow bodies therefore scale approximately as the square of the slope scale $m^{1.6}$.

3.3. The steep limit

Let us now consider the converse limit of steep surfaces, $h_x \gg 1$, given by $m \rightarrow \infty$. In this limit, the along-slope component of gravity acts vertically to leading order with negligible dependence on the slope, with $\sin \alpha \approx 1$ and $s_x \approx |h_x|$. In this limit, the governing equation (2.16) simplifies to

$$\frac{\partial h}{\partial t} = \frac{-A|h_x|}{\left(\int_0^x |h_x| dx\right)^{1/4}}, \quad (3.14)$$

forming a steep version of the theory. In this case, the dissolution pattern is given by $V \approx A[h_0(t) - z]^{-1/4}$, where $h_0(t)$ is the tip position, as derived from (2.15) on setting $\alpha \approx \pi/2$. Thus, the dissolution pattern does not depend on the slope h_x at leading order. However, a non-trivial time-dependence of the problem is retained in the coupling between dissolution and the tip position $h_0(t)$. To see this explicitly, it is helpful to recast the evolution equation (3.14) in terms of the horizontal position of the boundary, $x = X(z, t)$, which yields

$$\frac{\partial X}{\partial t} = -V = \frac{-A}{(h_0(t) - z)^{1/4}}, \quad \text{where } X(h_0, t) = 0. \quad (3.15a,b)$$

Thus, the dissolution pattern evolves in response to descent of the tip $h_0(t)$ which is, in turn, coupled to the surface profile via (3.15b).

The similarity form of (3.14), along with (3.4b), yields the reduced system

$$\frac{4}{5}(f - \xi f') = \frac{-|f'|}{\left(\int_0^\xi |f'| d\xi\right)^{1/4}}, \quad f(\infty) \sim -m\xi. \quad (3.16a,b)$$

Recasting these equations in terms of the new set of variables

$$\eta = m^{1/5}\xi, \quad \phi = m^{-4/5}f, \quad (3.17)$$

we obtain

$$\frac{4}{5}(\phi - \eta\phi') = \frac{-|\phi'|}{\left(\int_0^\eta |\phi'| d\eta\right)^{1/4}}, \quad \phi(\infty) \sim -\eta. \quad (3.18a,b)$$

The new system above is independent of m , implying that there exists a universal limiting steep solution subject to scaling. This solution can be determined analytically (appendix E) as

$$\frac{4}{5}(-\phi_0)^{1/4}\eta = \frac{\phi}{\phi_0} \int_1^{\phi/\phi_0} \frac{\chi^{-2}}{(\chi - 1)^{1/4}} d\chi, \quad (3.19)$$

where $\phi_0 = -(5\pi/8\sqrt{2})^{4/5} \approx -1.300$ is the prefactor to the descent position. The solution (3.19) is plotted in terms of the original similarity coordinates (ξ, f) as a dashed blue curve in figure 6(a) where, at the scale shown, it effectively overlays the full numerically determined solution shown as a solid black curve. The implied asymptote for the descent position and sharpness prefactor (3.6) are therefore

$$f_0 \sim 1.300 m^{4/5}, \quad \Sigma = 0.878 m^{16/5}, \quad (3.20a,b)$$

respectively. The descent position (3.20a) is shown as a dashed black line in figure 3(b), and matches the numerically determined prefactor for $m \rightarrow \infty$. The result of (3.20b) implies a rapid near cubic increase of the sharpness with the slope scale $m^{3.2}$, implying a particularly rapid increase in tip sharpness with the initial slope.

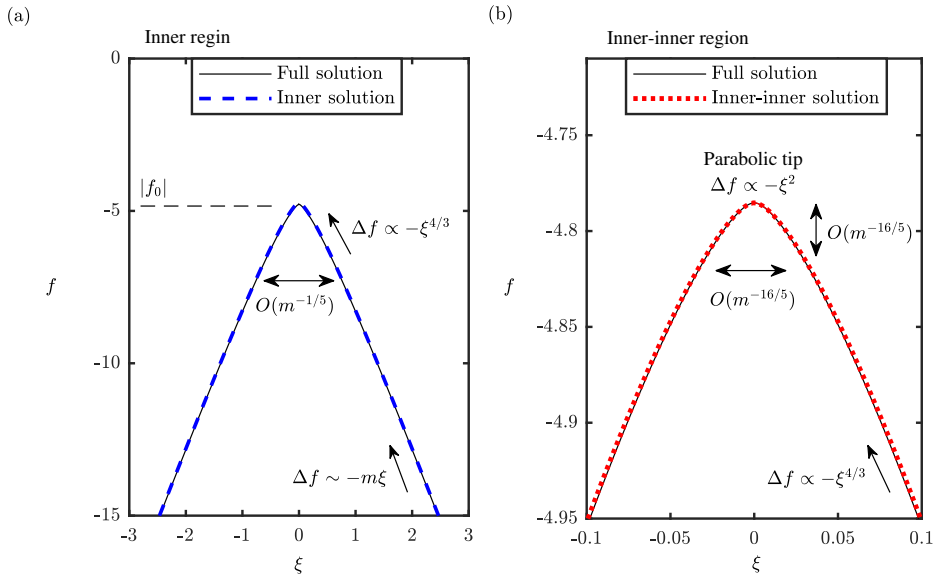


FIGURE 6. The asymptotic structure of the steep similarity solutions, as detailed in section 3.3, shown for the illustrative steep case $m = 5$. The plots show, at different scales, the full numerical solution to (3.4) (black solid curve). In panel (a), the inner solution to (3.19) (dashed blue curve) is compared alongside the full numerical solution at a large scale, illustrating the transition over a region of $O(m^{-1/5})$ from an outer region wherein the shape asymptotes towards the initial profile to a region in which the shape assumes a 4/3-power. In panel (b), the full solution is compared alongside the solution to the inner-inner (3.24) (red dotted curve). Through this inner-inner sublayer, the profile transitions from the 4/3-power shape to a parabola on a scale of $O(m^{-16/5})$. The variable $\Delta f(\xi) = f(\xi) - f_0$ represents the shape of the body zeroed at the tip, where $f_0 = f(0)$. In plotting the inner-inner solution, we have chosen to fix the reference tip position f_0 using the numerically determined solution, in order to show a clear comparison between the near-tip shape of the inner-inner region and the numerical solution in panel (b).

According to (3.19), the shape near the tip is given by

$$\phi \sim \phi_0 - \left(-\frac{3}{5}\phi_0\eta\right)^{4/3} \quad (\eta \rightarrow 0), \quad (3.21)$$

indicating a 4/3-power shape. The result of (3.21) implies infinite tip sharpness ($\phi''(0) = \infty$) and appears to conflict with the general property derived in section 2.2 that the tip is parabolic. The discrepancy arises because the assumption of a steep slope ($h_x \gg 1$) underlying (3.19) and (3.21) breaks down as $\eta \rightarrow 0$ as the profile transitions to being locally horizontal. Indeed (3.21) predicts that $\phi' \rightarrow 0$ as $\eta \rightarrow 0$, self-contradicting the assumption that $h_x \gg 1$ that underlies it. The steep limit $m \rightarrow \infty$ is therefore singular.

3.3.1. Matching to the parabolic tip through an inner non-steep region

To resolve the conflict between (2.18) and (3.21), we consider an asymptotic sublayer near the tip through which we allow the surface to be non-steep, $|h_x| \sim 1$. Let $\eta \sim \varepsilon(m)$ denote the as-yet-undetermined horizontal extent of this non-steep sublayer. Recasting the full similarity equation (3.4) in terms of the steep similarity variables (3.17), but now retaining all the terms, we obtain

$$\frac{4}{5}(\phi - \eta\phi') = \frac{-|\phi'(m^{-2} + \phi'^2)|^{1/3}}{\left(\int_0^\eta |\phi'(m^{-2} + \phi'^2)|^{1/3} d\eta\right)^{1/4}}. \quad (3.22)$$

Here, the m^{-2} terms can be interpreted as the non-steep correction to the steep solution (3.19), with these terms intervening wherever $\phi' \lesssim m^{-1}$. Neglect of the m^{-2} terms in (3.22) indeed recovers (3.18). To determine the size of the non-steep sublayer, we note that the steep outer (3.21) predicts its own inconsistency once $\eta \sim m^{-3} \equiv \varepsilon$. The relevant inner-inner coordinate ζ and variable ψ can now be written down as

$$\eta = m^{-3}\zeta, \quad \phi = \phi_0 + m^{-4}\psi(\zeta), \quad (3.23)$$

where the latter follows on considering where $\phi' \sim m^{-1}$. Substituting (3.23) into (3.22) and neglecting higher-order terms, we obtain the inner-inner equation

$$\frac{4}{5}\phi_0 = \frac{-|\psi'(1 + \psi'^2)|^{1/3}}{\left(\int_0^\zeta |\psi'(1 + \psi'^2)|^{1/3} d\zeta\right)^{1/4}}. \quad (3.24)$$

The single neglected term in this inner equation compared to the full equation (3.22) is the $\eta\phi'$ term. Thus, the solution undergoes an asymptotic transition from an outer steep region that is simplified by neglect of the non-steep correction m^{-2} , to an inner non-steep region that is simplified by neglect of the $\eta\phi'$ term.

The solution to the inner (3.24) provides the universal form of a tip matching to a steep body upstream. The solution to (3.24) for $\psi(\zeta)$ was determined numerically using a modification of our numerical scheme used for (3.4). To illustrate the general asymptotic structure, we show in figure 6, at two levels of magnification, the full numerical solution to (3.4) for $m = 5$ (black solid curve), plotted in terms of the original similarity variables (ξ, f) . In panel (a), the full solution is compared alongside the inner solution (3.16) (blue dashed curve). In panel (b), the full solution is compared with the inner solution to (3.24) (red dotted curve). To provide an effective comparison of the near-tip shape in the inner-inner region in panel (b), we set the height of the tip of the inner-inner solution to coincide with that of our numerically determined value of f_0 . The plot shows the switch from the intermediate 4/3-shape in the inner limit of the inner solution (3.19) to a parabola near the tip. In terms of the original similarity variables, the size of the non-steep zone at the tip, derived using (3.23) and (3.17), has equivalent horizontal and vertical dimensions given by $\xi \sim m^{-16/5}$. The 4/3-power intermediate shape (3.21), applicable over the region $m^{-16/5} \ll \xi \ll m^{-1/5}$, is a factor of m^3 larger than the parabola in $\xi \ll m^{-16/5}$.

4. Axisymmetric bodies

The dissolution of axisymmetric bodies is governed by different equations and produces different similarity solutions. We define the surface of an axisymmetric body by $z = h(r, t)$, where r is the horizontal distance from the vertical axis of the body. The boundary-layer equations describing axisymmetric natural convection read (Merk & Prins 1953)

$$\frac{\partial(ru)}{\partial s} + \frac{\partial(rv)}{\partial y} = 0, \quad (4.1)$$

$$\rho \left(u \frac{\partial u}{\partial s} + v \frac{\partial u}{\partial y} \right) = \frac{\partial}{\partial y} \left(\mu \frac{\partial u}{\partial y} \right) + \Delta \rho g \sin[\alpha(s, t)]C, \quad (4.2)$$

$$u \frac{\partial C}{\partial s} + v \frac{\partial C}{\partial y} = \frac{\partial}{\partial y} \left(\kappa \frac{\partial C}{\partial y} \right), \quad (4.3)$$

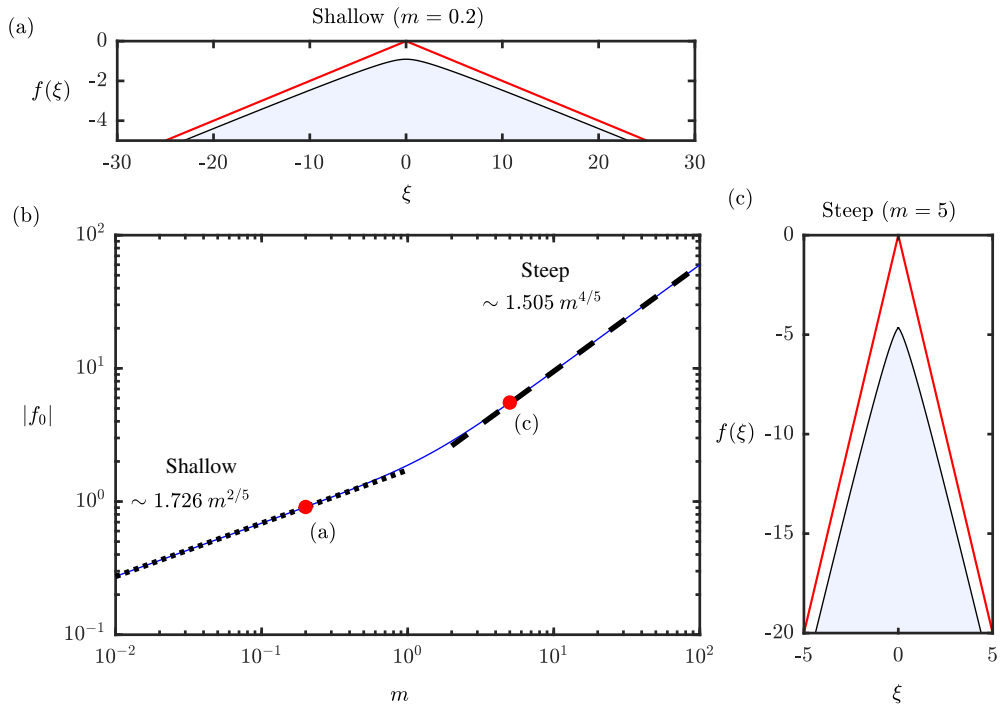


FIGURE 7. Similarity solutions describing the shape evolution of an initially axisymmetric conic body, determined by numerically solving the ordinary integro-differential system (4.8). Panels (a) and (c) show the solutions for the shallow case $m = 0.2$ and the steep case $m = 5$, respectively. Panel (b) shows the general relationship between tip-descent prefactor $|f_0|$ and the slope m for an initially conic body. The asymptotes in the limits of $m \rightarrow 0$ and $m \rightarrow \infty$ are shown as a black dotted line and a black dashed line, respectively, as predicted by the reduced asymptotic models derived in section 4. The locations of the examples in (a) and (c) are indicated by red circles. The solutions are determined by numerically solving the ordinary integro-differential system (4.8), forming the axisymmetric analogue of figure 3.

where the coordinate system (s, y) is defined similarly to that used for the two-dimensional case, with s representing the arc length moving radially along the outside of the body, and y the normal distance from the surface. The only difference between these equations and those of (2.9)–(2.11) is the presence of r in (4.1). One interesting implication is to introduce a new dependence of the boundary-layer system on the surface profile within the governing boundary-layer system. Even for steep bodies, an axisymmetric dissolution pattern depends on the shape profile and not only the tip position, as applied in the two-dimensional case (3.15). The presence of r in (4.1) also precludes the transformation of Acrivos (1960a) from eliminating the surface profile, as was required to derive the dissolution pattern (2.15) (appendix C). However, it is possible to transform the axisymmetric equations first onto a new system (Mangler 1948) that is equivalent in mathematical form to the two-dimensional equations. On applying these transformations, and then recasting the surface mass diffusion rate back in terms of the original variables (appendix F), the axisymmetric analogue of (2.14) is determined as

$$q = \frac{D(r \sin \alpha)^{1/3}}{\left(\int_0^s (r^4 \sin \alpha)^{1/3} ds\right)^{1/4}}, \quad (4.4)$$

derived in Acrivos (1960*b*). Compared to its two-dimensional analogue (2.14), this equation includes new dependences on the radial coordinate r representing the effects of radial spreading.

Substituting (4.4) into (2.7), we obtain the new asymmetric model for shape evolution

$$h_t = \frac{-A|r h_r s_r^2|^{1/3}}{\left(\int_0^r |r^4 h_r s_r^2|^{1/3} dr\right)^{1/4}}, \quad s_r = \sqrt{1 + h_r^2}, \quad (4.5)$$

forming the axisymmetric version of (2.16). The structure of (4.5) is similar to the two-dimensional equation (2.16), with the exception that it includes new factors of r representing the effects of radial spreading. These new factors cancel in a scaling sense, implying that all the fundamental similarity scalings discussed in section 3.1 are preserved. Indeed, this could have been anticipated since the original introduction of r in (4.1) did not introduce any new scalings into the problem. Although the presence of r does not alter the fundamental temporal scales of evolution, it does alter the cross-section shapes of the evolving body.

Repeating the analysis of the admissible tip shape and tip-descent rate conducted in section 2.2 for the axisymmetric equation (4.5), we obtain the near-tip ($r \rightarrow 0$) asymptotic shape

$$h \sim h_0(t) - \frac{1}{2}S(t)r^2. \quad (4.6)$$

Thus, the shape of an axisymmetric tip dissolving under buoyancy is paraboloidal. Moreover, we obtain the axisymmetric tip-descent law

$$\frac{\partial h_0}{\partial t} = -A \left(\frac{8}{3}S(t) \right)^{1/4}. \quad (4.7)$$

The prefactor to the tip-descent law (4.7) is a factor of $2^{1/4} \approx 1.2$ larger than that of the corresponding two-dimensional result of (2.17), implying that axisymmetric tips dissolve approximately 20% faster for the same cross-sectional tip curvature $S(t)$.

To determine the shape functions of the axisymmetric similarity solutions, we recast (4.5) in terms of the similarity variables, $r = (At)^{4/5}\xi$ and $h(r, t) = (At)^{4/5}f(\xi)$, giving

$$\frac{4}{5}(f - \xi f') = \frac{-|\xi f' s'^2|^{1/3}}{\left(\int_0^\xi |\xi^4 f' s'^2|^{1/3} d\xi\right)^{1/4}}, \quad f(\infty) \sim -mr, \quad (4.8a, b)$$

forming the axisymmetric analogue of (3.4). We solve this equation using a modification of the numerical scheme used for (3.4) to incorporate the new ξ terms. The resulting shape functions for cones of initial slope $m = 0.2$ and 5 are shown in figure 7(*a, c*). The shapes are qualitatively similar to those found for the two-dimensional solutions shown in figure 3. The most appreciable difference is the alteration of the descent prefactor $|f_0|$ shown in figure 7(*b*). The descent prefactor is, across the complete range of m , a near-universal factor of ≈ 1.16 larger than those of the corresponding two-dimensional values of $|f_0|$ shown in figure 3(*b*). Axisymmetric bodies thus dissolve approximately 16% faster for the same slope scale m . The similarity form of the tip-descent law (4.7) is given by

$$\Sigma = \frac{3}{8} \left(\frac{4}{5}f_0 \right)^4, \quad (4.9)$$

which is one half the value of the two-dimensional analogue (3.7). Axisymmetric tips are therefore half as sharp as two-dimensional tips with the same descent prefactor f_0 .

We develop shallow and steep asymptotic limits as follows. The limit of a shallow

axisymmetric body ($h_r \ll 1$) yields

$$\frac{4}{5} (f - \xi f') = \frac{-|\xi f'|^{1/3}}{\left(\int_0^\xi |\xi^4 f'|^{1/3} d\xi\right)^{1/4}}. \quad (4.10)$$

Following the same rescaling of (3.11), we obtain $\phi_0 \approx -1.726$. The associated asymptote $f = -1.726 m^{2/5}$ is shown as a dotted line in figure 7(b), and accurately represents the small- m limit for $m < 0.5$.

The corresponding similarity equation in the steep limit ($h_r \gg 1$) is given by

$$\frac{4}{5} (f - \xi f') = \frac{-\xi |f'|}{\left(\int_0^\xi \xi^4 |f'| d\xi\right)^{1/4}}. \quad (4.11)$$

Unlike the two-dimensional case, the steep axisymmetric model of (4.11) cannot be integrated analytically. This is a reflection of the fact that the axisymmetric dissolution pattern depends on the surface profile as a consequence of radial spreading from the tip. Recasting (4.11) in terms of the scaled variables (3.17) and solving the resulting system numerically, we obtain the universal steep solution applicable to an axisymmetric body. The resulting prefactor is $\phi_0 \approx 1.505$ and hence $f_0 \sim 1.505 m^{4/5}$, which is shown as a dashed black line in figure 7. Trying a power-law solution of the form $\phi = \phi_0 + c\eta^\alpha$ in (4.11) and taking the limit $\eta \rightarrow 0$, we obtain

$$\phi \sim \phi_0 - \left(-\frac{3}{5\sqrt{2}}\phi_0\eta\right)^{4/3} \quad (\eta \rightarrow 0), \quad (4.12)$$

forming the modified axisymmetric analogue of (3.21). Thus, the shape of a steep axisymmetric body also forms a 4/3-power in the lead-in to the tip with a slightly modified prefactor. To resolve the transition to a parabolic tip with a finite sharpness prefactor (3.20), one could construct the same kind of asymptotic framework as was done in the two-dimensional case in section 3.3.1. The same essential scalings for the size of the inner non-steep region arise, and thus we omit the analysis here for brevity.

5. Laboratory study

In order to test the predictions of our theoretical model, we conducted a series of laboratory experiments. For this, we used bodies of solidified sugar (known as rock candy or boiled sweets) immersed in freshwater, as illustrated schematically in figure 8 and as a sequence of photographs in figure 9. The experiment was contained in a square-based tank of length 62.5 cm, width 62.5 cm and height 61 cm. The tank was backlit using LED light tape. The top of the tank was covered to suppress evaporative cooling. The water temperature was measured during experiments using an alcohol thermometer inside the tank. The temperature remained between 23 and 25 °C during each experiment.

The candy was made from an 8:3:2 volume mixture of sugar, corn syrup, and water, and coloured using blue food dye. The mixture was heated to 150 °C, representing the ‘hard crack’ temperature at which the solution has crossed the glass transition and will set as solid candy. The molten candy was then sand cast, using a plastic conic mould and left to cool and harden.

In order to prevent the candy from moving or rocking over the course of the experiment, the base of each cone was glued to a plastic dish (10 cm diameter) using silicone sealant. The dish was rested on a raised stand 12 cm from the base of the tank for the relatively shorter cones used for experiments A and B, and a piece of PVC to a height of 2.5 cm

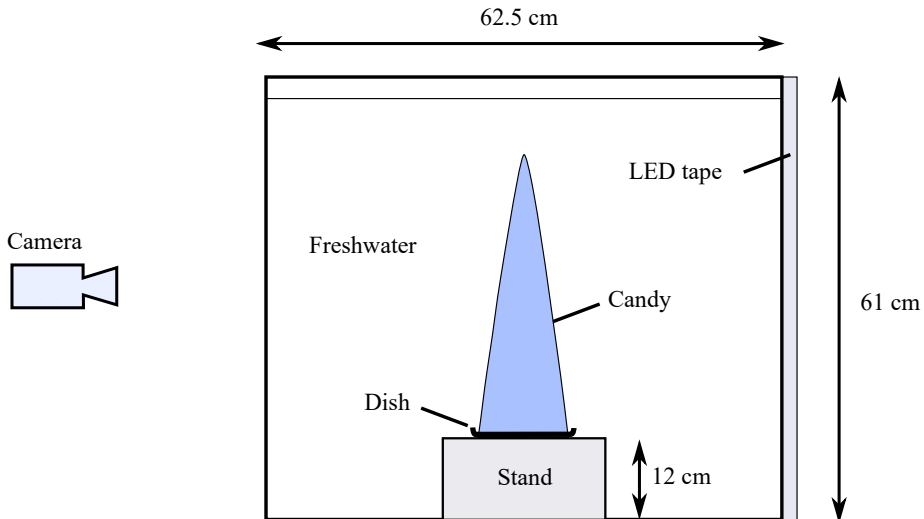


FIGURE 8. Schematic of our experimental apparatus, as described in section 5. An alcohol thermometer was used to measure the temperature of the water inside the tank. The top of the tank was covered to suppress evaporative cooling during experiments. Two stands were used to raise the candy cone off the floor of the tank: the one illustrated in this figure was 12 cm high and was used for the relatively shorter cones used for experiments A and B, whereas a stand of 2.5 cm was used for the relatively taller cones used for experiments C and D. The stand was used to create a space for the heavy solution to collect at the floor of the tank so that the candy remains immersed in fresh ambient fluid.

| Experiment | m | A ($\text{cm}^{5/4} \text{s}^{-1}$) |
|------------|-------|---|
| A | 5.78 | $(1.60 \pm 0.04) \times 10^{-4}$ |
| B | 10.77 | $(1.41 \pm 0.05) \times 10^{-4}$ |
| C | 12.33 | $(1.57 \pm 0.05) \times 10^{-4}$ |
| D | 17.62 | $(1.54 \pm 0.33) \times 10^{-4}$ |

TABLE 1. The initial slope m and convective strength A for each of our experiments. The bounds on A represent twice the standard deviation of values of the set of values of A inferred over the course of each experiment, as described in section 5 and illustrated in figure 10.

for the relatively taller cones used for experiments C and D. This was done in order to provide a region below the base of the cone where dissolved sugar can collect, thus suppressing the development of a stratification above the base of the cone that would change the ambient conditions. The experiment was recorded using a camera facing the front of the experimental tank with photographs taken at regular intervals of 30 seconds.

The convective strength A was estimated for each experiment by measuring the spatial pattern of the rate of change of the surface position in the horizontal direction, $V_r \equiv$

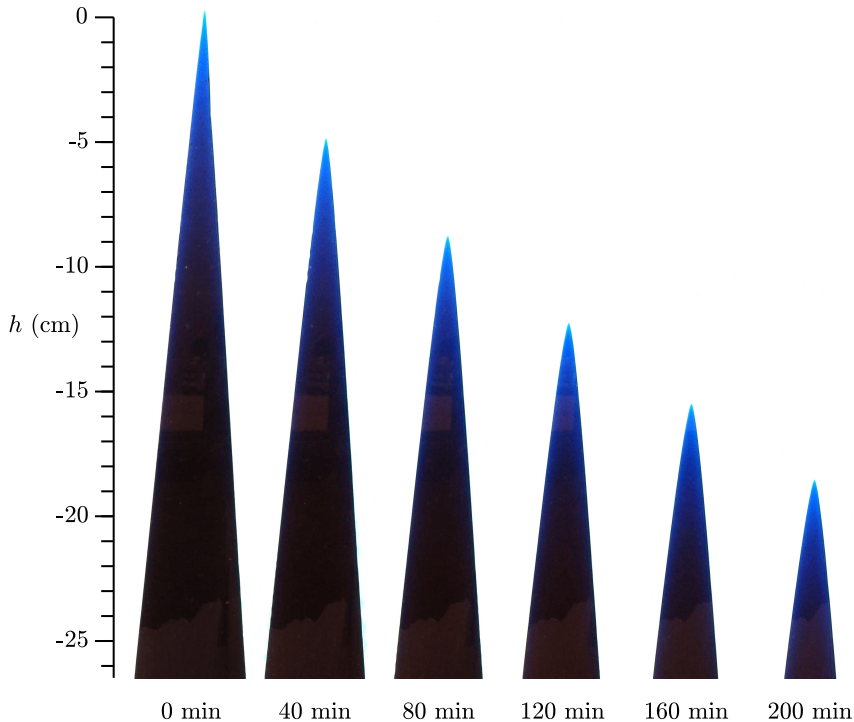


FIGURE 9. Dissolution of a candy cone at 40-minute intervals, illustrating the descent of the tip. The images are from experiment C, which had an initial slope of $m = 12.3$. A scale bar is provided on the left, indicating descent rates of several cm per hour. A video of this experiment is included as supplementary information.

$|\mathbf{V} \cdot \mathbf{e}_x|$. As illustrated for experiment C in figure 10, the profiles of $V_r(z, t)$ collapse together onto a curve that remains approximately steady in time. For a near-conic surface, (4.4) predicts a dissolution pattern of the form

$$V_r = A_c [h_0(t) - z]^{-1/4}, \quad (5.1)$$

where A_c satisfies

$$A = \left(\frac{3}{7}\right)^{1/4} (\sin \alpha)^{-3/2} A_c, \quad (5.2)$$

and $\sin \alpha = m/\sqrt{1+m^2}$. The experimental value of A is inferred by fitting (5.1) to the measured dissolution profiles. The resulting curve for experiment C is illustrated by the black dashed curve in figure 10. The experimental dissolution patterns sampled at regular time intervals show good agreement with the predicted pattern of (5.1). For each sampled time, we obtained an empirical estimate of the prefactor A_c and hence the convective strength A via (5.2). A single value of A for each experiment was evaluated by averaging the sampled values. A slight variation in the value of A between different experiments shown in table 1 was likely caused by slight differences in temperature, or an effect of slight non-axisymmetry caused by some leaning of the cone.

5.1. Experimental results

We performed four experiments spanning initial cone slopes m from 5.8 to 17.6 and convective strengths A from 1.4×10^{-4} to $1.6 \times 10^{-4} \text{ cm}^{5/4} \text{ s}^{-1}$, as listed in table 1. Due to small errors in alignment, the cones were angled slightly with respect to gravity (by

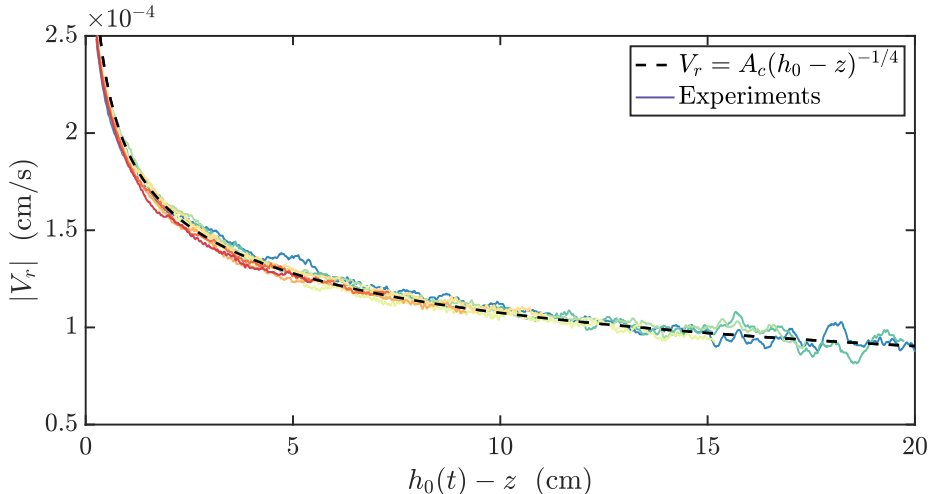


FIGURE 10. The horizontal velocity of the surface of the candy, V_r , as a function of distance below the tip ($h_0(t) - z$) for a selection of sampled times over the course of experiment C (coloured solid curves). The horizontal velocity was evaluated using the formula $V_r(z) = \Delta r / \Delta t$, where $\Delta r(z)$ is the horizontal difference in surface profiles between the profiles at times t and $t + \Delta t$, where $\Delta t = 5$ min. The value of $|V_r|$ is found for both the left and right side of the shape separately and then averaged. The function (5.1) is fitted to each time with A_c and h_0 treated as fitting coefficients. The dashed line represents the curve produced by the mean value of the values obtained from the individual sampled times, yielding the values listed in table 1.

< 1 degree). In order to correct for small variations in each experiment in the angle of the cone with respect to the camera, the images were rotated by a small angle (around a 1 degree) such that the cone is oriented vertically in the frame of each image. A sequence of images from experiment C are shown in figure 9, illustrating descent rates of a few cm per hour. Videos of each of the four experiments are included as supplementary information.

The profiles of the solid boundaries were extracted digitally from the experimental images using a thresholding method of the red channel of the RGB images. The evolution of the extracted profiles is shown in the left-hand column of figure 11 with each row representing a different experiment listed in table 1. The profiles are observed to produce relatively smooth shapes that descend with time. In experiment D, a localised notch in the side of the candy was found to grow and eventually cause the tip to break off, as shown in figure 11(d). We believe this phenomenon to be associated with a localised instability whereby a small notch in the side of the dissolving shape rapidly grows in response to accelerated dissolution along the underside of the notch. This may be related to the instability mechanism giving rise to pits on the underside of melting or dissolving bodies (e.g. Vanier & Tien 1970; Kerr 1994; Mcleod *et al.* 1996; Sullivan *et al.* 1996; Davies Wykes *et al.* 2018). Despite the emergence of this feature, we have nonetheless retained this experiment to illustrate the phenomenon, as well as to show that the descent of the tip is, before the notch extends across the width of the candy, largely unaffected by its emergence.

Naturally, the initial experimental shapes were not perfect cones. In particular, experiments B and D began with relatively blunted tips. To draw a fairer comparison between experiments in view of these blunted tips, we chose the reference height $z = 0$ and time origin $t = 0$ such as to be consistent with the assumed initial condition of the similarity solution. For this, the location of $z = 0$ was set as the height of the intersection of two lines fitted to either side of the initial shape, corresponding to the initial position

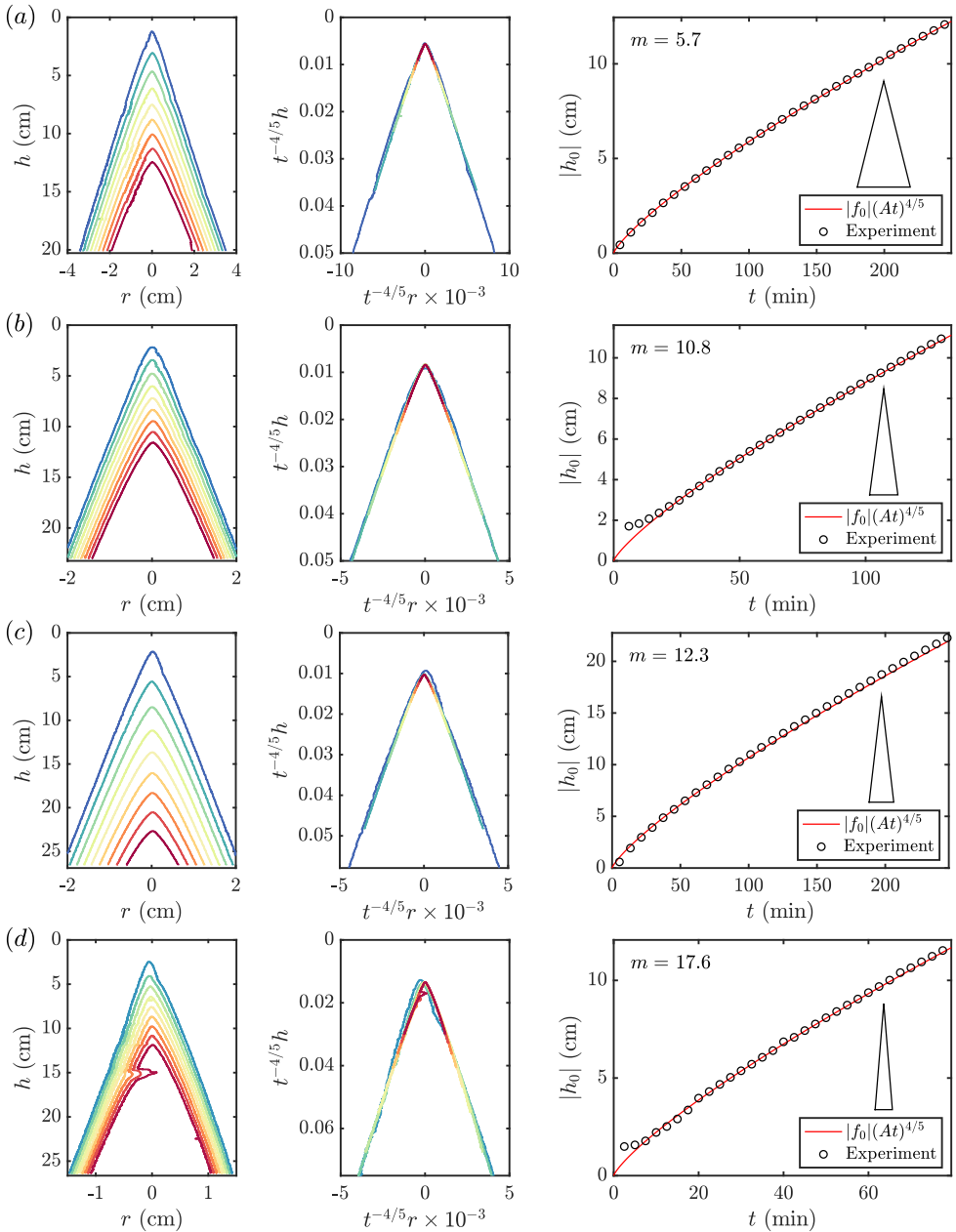


FIGURE 11. Experimental results of dissolving candy cones. Successive rows represent experiments A–D, as listed in table 1, corresponding to slopes of (a) $m = 5.8$, (b) $m = 10.8$, (c) $m = 12.3$, and (d) $m = 17.6$. The left-hand column shows the evolution of the shape extracted digitally from our recordings. The central column shows the same profiles in a coordinate system in which the horizontal and vertical dimensions are each rescaled by $t^{4/5}$. The right-hand column shows the experimental tip position against time (circles) and the associated theoretical prediction (5.3) (red solid line), where a time shift has been applied to account for the fact that the initial shapes are not perfect cones. Insets in the right-hand column show the outlines of the initial shapes for each experiment, illustrating the varying steepnesses.

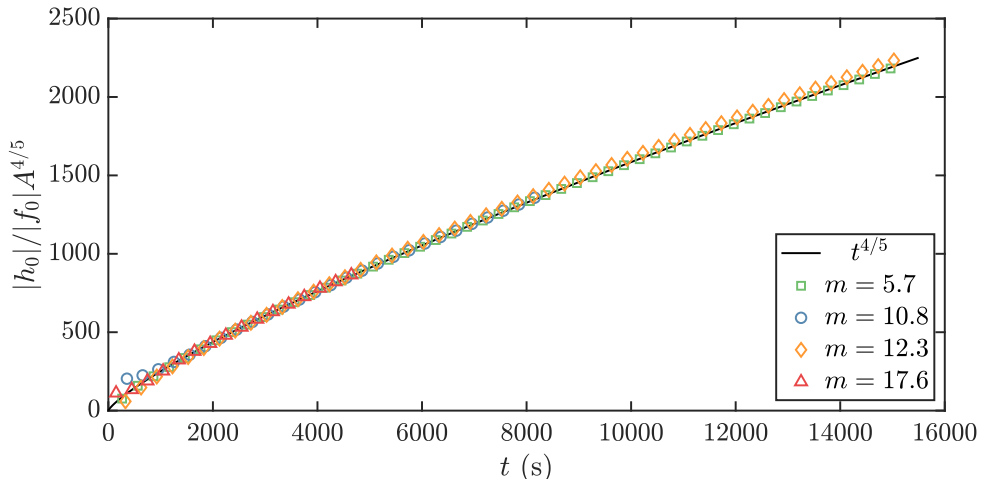


FIGURE 12. Collapse of the tip position from all four of our experiments onto a universal curve. The experimental tip positions $|h_0(t)|$ (shown as symbols) are normalised by the quantity $|f_0|A^{4/5}$, where $|f_0| = 1.505 m^{4/5}$, which, according to the theoretical prediction (5.3), should collapse onto the universal curve $t^{4/5}$ (shown as a black solid curve). A time shift has been applied to each experiment to account for the fact that the initial shapes were not perfect cones. An error estimate was evaluated as twice the error associated with the measurement of A (shown in table 1). The error range was smaller than the sizes of the symbols, and has thus been omitted.

of the tip that would apply if the initial shapes were perfectly conic. To allow for small variations between the time that the cones were placed in the tank and the time at which the first images were taken, the time origin was selected by picking a single measurement of the tip height h_0 for each experiment and requiring that $t = (h_0/f_0)^{5/4}/A$. The time chosen for this was 30 minutes after each experiment was initialised. Increasing this time made no appreciable difference to the inferred time origin. The inferred time origins were 2 to 6 minutes before the first image was taken.

As an initial test, we examine whether the experimental shapes collapse onto a self-similar shape on suitable stretching of the coordinates in terms of our similarity variables (3.3). According to the theory, the shape evolves as

$$h(r, t) = (At)^{4/5} f\left(\frac{r}{(At)^{4/5}}\right), \quad (5.3)$$

where $f(\xi)$ is a shape function determined theoretically in section 4. Therefore, if the vertical and horizontal coordinates are both rescaled by $t^{-4/5}$, the outlines of the body should collapse to lie on top of one another. To test this collapse, we plotted the outlines of the experimental shapes with the horizontal and vertical dimensions both scaled by $t^{4/5}$. As shown in the central column of figure 11, each outline collapses to excellent approximation onto a shape that is fixed with respect to the rescaled coordinates. This confirms the essential self-similarity predicted by the theory.

Next, we present direct comparisons between the theoretical prediction for the tip evolution $h_0(t)$ and the experimental results. The theory of section 4 predicts that the tip descends according to

$$h_0(t) = f_0(At)^{4/5} = -1.505 m^{4/5} (At)^{4/5}, \quad (5.4)$$

where, in view of the steepness of our experiments ($m > 5.8$), we have in the second equation used the prefactor that applies to the limiting steep theory (3.20a).

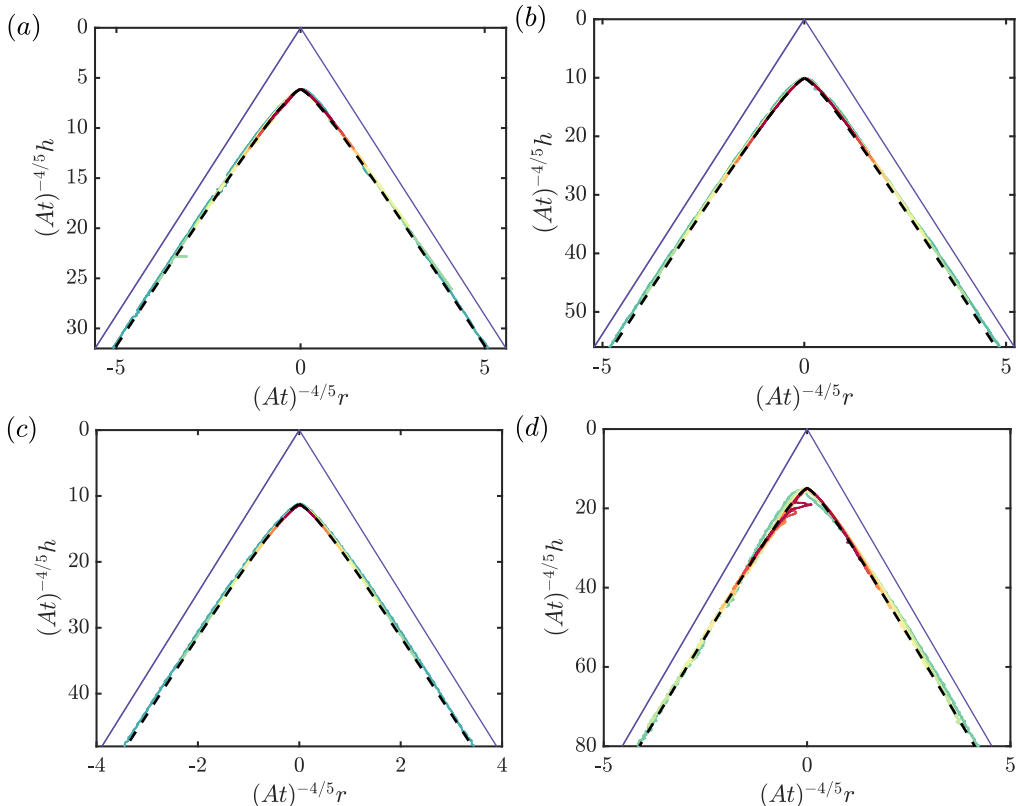


FIGURE 13. Experimental profiles rescaled into similarity variables, $\xi = (At)^{-4/5}r$ and $f(\xi) = (At)^{-4/5}h(r, t)$, for each of our experiments A to D. The theoretical prediction (5.3) is shown as a dashed black curve in each case, with $f(\xi)$ is determined by solving (4.8) using the value of m relevant to each experiment. There is a generally good collapse of the experiments onto the theoretically predicted self-similar shape. With the exception of the choice of time origin, no adjustable parameters were used to formulate this comparison. The initial theoretical shape is shown by the solid blue lines in each case.

The tip positions of each experiment inferred using the thresholding method are plotted as functions of time in the right-hand column of figure 11. In each case, we have overlaid the theoretical prediction of (5.3). Generally excellent agreement is observed. To test the universal collapse of the solutions, we have plotted each of the tip evolutions together in figure 12 in forms scaled by $|f_0|A^{4/5}$. According to the theoretical prediction of (5.3), the curves should, under this rescaling, all collapse onto the universal curve $t^{4/5}$. An excellent general collapse of the experiments onto this curve is found. With the exception of the choice of time origin used to account for the slightly non-conic initial shapes, no adjustable parameters have been used in this comparison. The agreement indicates that the general theoretical framework we have derived accurately captures the descent rates of dissolving bodies. The self-similar shapes predicted by the axisymmetric theory from section 4 are plotted alongside the collapsed profiles from each experiment A-D in the respective panels of figure 13. Again, there is an excellent agreement between experiment and theoretically predicted shapes.

6. Summary and discussion

We have developed a model describing the dissolution and melting of solid bodies under free convection that addresses the open question of the shapes formed by dissolving or melting bodies in the case of gravitationally stable free convection, and validated the predictions in the laboratory. Analysis of the model produces explicit predictions for the rates at which melting or dissolving shapes recede. The model development and demonstration of analytical approaches provides a basis for various generalisations of the model to understand dissolving shapes in more complicated and naturally occurring settings, a number of which will be discussed below. Our observed experimental shape profiles collapse to excellent approximation onto a consistent theoretically derived descent position and shape, giving confidence in the essential theoretical framework.

The models for both two-dimensional and axisymmetric bodies were derived by coupling the boundary-layer equations describing stable free convection to an evolution equation for the boundary. In the case of large- Sc number, the model was reduced further to a single integro-differential equation. Analysis of this equation shows that bodies comprised of intersecting planes or cones result in similarity solutions that ‘stretch’ in both the horizontal and vertical dimensions as $t^{4/5}$ with respect to the initial tip position. A general relationship between tip sharpness and descent rate was derived, showing that the tip is always parabolic sufficiently close to the tip and the descent rate is always proportional to the tip curvature to the one-quarter power.

Differing reduced asymptotic descriptions of shallow (near-horizontal) and steep (near-vertical) surfaces were derived. For shallow (near-horizontal) dissolving surfaces with initial slope m , the limiting parabolic tip occupies the region $x \ll m^{-3/5}(At)^{4/5}$. In the limit $m \rightarrow 0$, a full asymptotic description of the body surface $h(x, t)$ as a whole was derived (section 3.2), which is summarised by

$$(At)^{-1/5}h(x, t) \sim \begin{cases} f_0 - 0.75 m^{8/5} \xi^2 & \xi \ll m^{-3/5}, \\ m^{2/5} \phi(m^{3/5} \xi) & \xi = O(m^{-3/5}), \\ -m\xi & \xi \gg m^{-3/5}, \end{cases} \quad (6.1)$$

where $\xi = (At)^{-4/5}x$ is a scaled x -position, $f_0 = -1.49 m^{2/5}$, and ϕ is a universal (parameter-free) function. Shallow bodies thus form a parabolic region that matches to the initial shape far downstream over a length scale of order $m^{-3/5}(At)^{4/5}$.

For a steep body ($m \rightarrow \infty$), the shape instead forms a more intricate double-decked boundary layer structure containing both a parabolic and a $4/3$ -power near-tip region (section 3.3). The full structure is summarised by

$$(At)^{-1/5}h(x, t) \sim \begin{cases} f_0 - 0.44 m^{16/5} \xi^2 & \xi \ll m^{-16/5}, \\ f_0 + m^{-16/5} \psi(m^{16/5} \xi) & \xi = O(m^{-16/5}), \\ f_0 - 0.72 m^{16/75} \xi^{4/3} & m^{-16/5} \ll \xi \ll m^{-1/5}, \\ m^{4/5} \phi(m^{1/5} \xi) & \xi = O(m^{-1/5}), \\ -m\xi & \xi \gg m^{-1/5}, \end{cases} \quad (6.2)$$

where $f_0 = -1.30 m^{4/5}$, and ψ and ϕ are universal functions describing the inner-inner and inner decks, respectively (the function ϕ here differs from that of (6.1)). The ‘very’ near-tip limit of the inner-inner region, defined by $\xi \ll m^{-16/5}$, forms a parabolic shape. However, within the intermediate region between the inner and the inner-inner, the shape forms a $4/3$ power. The $4/3$ region is considerably larger than the parabolic region (it is a factor of order m^3 larger). Thus, while there are two near-tip limits in the case of steep

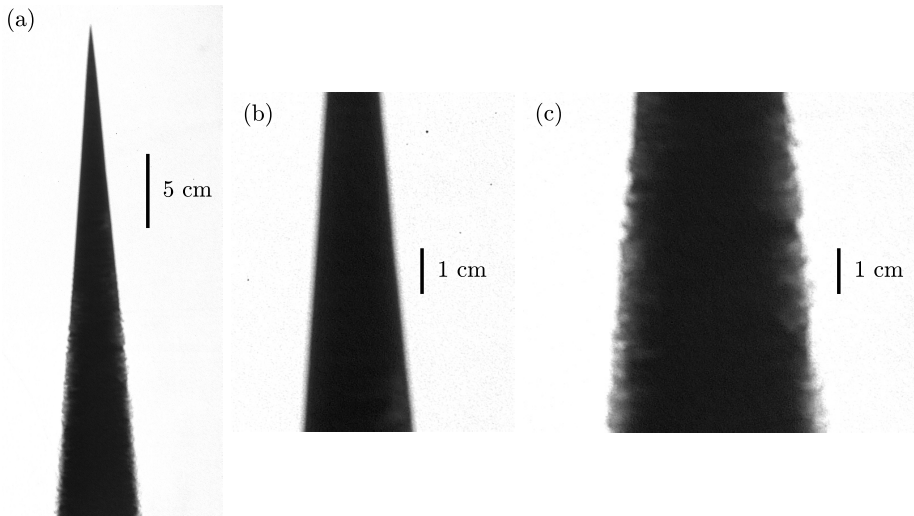


FIGURE 14. Shadowgraph image of dissolving candy cone. (a) A shadowgraph of experiment C ($m = 12.3$), (b) a section near the top of the cone, where the boundary layer cannot be seen as it remains laminar, and (c) shows a section lower down the cone, where intensity fluctuations suggest that the boundary layer has transitioned to turbulence. The image forms a still from a supplementary video, which illustrates the unsteadiness of the turbulent region.

bodies, the $4/3$ -shape applies over a much larger region, though the ultimate shape of the tip at the finest scale is parabolic.

The model and its predictions apply generally to situations where the viscosity, diffusivity and density are permitted to vary as any given functions of the concentration (or temperature in the case of melting). Even for mixtures with order-of-magnitude variations in fluid properties over the flow domain, the shapes produced are equivalent. For example, the shape evolution for a melting block of ice is the same as that which arises for a dissolving body of candy in water, despite the viscosity of the air remaining approximately constant in the case of an ice cube, but the viscosity of candy solutions varying by at least two orders of magnitude. The generality stems from a favourable property of similarity solutions in free convection that allows the effects of concentration-dependent properties to be encapsulated in the single parameter A . For this reason, equivalent shapes would even arise for two-component effects of compositional convection such as a block of ice melting in salty water, and for flows involving the reversal of buoyancy.

While, as noted above, the results do generalise to fluids with strongly concentration-dependent viscosity, one can question whether the generalisation applies for non-Newtonian fluid with a shear-dependent viscosity. The situation may apply, for example, to the case of a polymer dissolving under free convection into a solution with a different concentration. It was determined by Acrivos (1960*b*) that a direct generalisation of the result of (2.15) can be derived for power-law fluids. Therefore, a generalised form of the high-Schmidt number reduction of our model of the shape evolution (2.16) could be straightforwardly developed and analysed using the same techniques considered here. It can be anticipated that the self-similar shapes and temporal exponents of the descent rates associated with the similarity solutions would be altered.

The full model of (2.9)–(2.13) allows for the effects of inertia. However, our analysis focused on the predictions of a reduced model applicable under high Schmidt (or Prandtl) number, which affords the consideration of a purely viscous inner sublayer. The approx-

imation of neglecting inertia in fact remains good even for Schmidt numbers of order unity (Kuiken 1968), with only minor corrections to the thermal or mass transfer rates (the adjustment from the $Sc = \infty$ case is just $\approx 20\%$ for $Sc = 1$, for example). However, for situations where inertia may be required as a leading-order term in the solutal layer (e.g. for gases), the expression (2.15) can be anticipated to break down. In considering this case, we note that retaining the inertial terms introduces one new scaling into the system that is identical in form to the one already produced by scaling the advective and diffusive terms in (2.11), namely, $u/x \sim \nu/y^2$. Therefore, all the similarity scalings we derived from the simplified high- Sc number models of (2.16) or (4.5) will also apply generally with inertia, i.e. general Sc . While the similarity scalings for tip descent rates would be preserved (e.g. $h_0 \sim t^{4/5}$ for initially conic bodies), the introduction of inertia will alter the evolving shapes. The shapes could be determined by transforming the full model of (2.9)–(2.13) in terms of the similarity variables. The shape could then be determined using a one-off solution of the resulting two-variable heat equation in (ξ, y) . Thus, similarity solutions still exist for general Sc , but require the consideration of a two-variable system in (ξ, y) , rather than the purely ordinary system of the form (3.4) that applies in the large- Sc limit.

An overarching assumption in our analysis is that the boundary layer remains laminar. If the boundary-layer flow becomes unstable and transitions to turbulence, the rates and profiles of convective transfer at the interface will differ from what we have assumed. We were surprised to find that this transition occurs even in the relatively viscous context of our laboratory experiments, as shown in the shadowgraph of one of our experiments in figure 14. Panel (c) illustrates the development of a regular pattern of convective rolls which flow along the surface of the body, characterised by a much thicker boundary-layer region compared to the laminar region shown in panel (b). Experiments of turbulent composition free convection of ice melting into ambient salty water (Kerr & McConnochie 2015; McConnochie & Kerr 2018) indicate that the rate of heat or solutal transfer in this regime becomes independent of the distance moved downstream of the body, but still depends on the local slope. It is anticipated that an evolution equation analogous to the kind we have developed (2.16) could be derived to couple a transfer law applicable to turbulent free convection to the shape evolution and analysed to derive shape evolutions in this case. The result would likely reveal different shapes and descent laws to those we have reported here. Recent research has also considered the different turbulent regime of a plume flowing along the underside of an ice shelf and maintained by a constant source of buoyancy at the grounding line by an input of relatively fresh subglacial discharge (e.g. Dallaston *et al.* 2015; Slater *et al.* 2017; Hewitt 2020). This regime differs in being driven by the introduced buoyancy flux as opposed to the cooling by the wall, but similarly results in the potential for interplay between buoyancy-driven flow and shape evolution.

We speculate that an adaptation of the model could be developed to describe the evolution of solidifying bodies under free convection. A situation of this kind has been used to model the growth of icicles (Makkonen 1988; Short *et al.* 2006; Camporeale & Ridolfi 2012). In this situation, a thin film introduced at the top of the icicle flows down along its exterior and freezes at a spatially variable rate controlled by an upwelling convective boundary layer generated by latent heating (Makkonen 1988). By imposing a constraint that the shape of the growing icicle remains preserved, Short *et al.* (2006) derive a solution that asymptotes to a $4/3$ -power shape far away from the tip. This form of shape is interpreted as a far-field asymptote in this case, contrasting with our prediction of (4.12) that a $4/3$ -power shape applies in a limit close to the tip. Analysis of the formation of dendrites in the (non-fluid-mechanical) context of a two-dimensional solid solidifying into an ambient under thermal diffusion has revealed the development

of parabolic solutions (Nash & Glicksman 1979; Ivantsov 1985). Similarity with the parabolic regimes we identify appears to be incidental because the formation of the parabola in the context of our results is due to an inherent fluid-mechanical property of free-convective boundary layers that the parabola is the unique shape for which the boundary layer predicts a locally smooth recession rate. In principle, our model could be adapted to describe a solidifying body under free convection, and would likely require additional physics such as surface tension in order to suppress morphological instabilities.

The model we have considered has focused on the case of a purely free-convective (buoyancy-driven) boundary layer. We have neglected any effect of an externally imposed flow, i.e. forced convection, which has been investigated by others (Moore *et al.* 2013; Moore 2017; Huang *et al.* 2015). In many naturally occurring problems involving melting bodies, such as icebergs (e.g. FitzMaurice *et al.* 2017), it can be anticipated that a mixture of forced convection and natural convection can both contribute. Our analysis has addressed one limit of this spectrum. Future theoretical work could consider the extension to allow for mixed (forced and free) convection, potentially with the two acting in differing directions on the body (as considered experimentally by Hao & Tao 2001, 2002). For the context of the shaping of rock spires, the buoyancy-driven dissolution may take the form of a thin-layer flow fed at a constant flux (rainfall) over the surface. This situation creates a buoyancy-driven gravity current over the surface fed by source conditions, a case which could be addressed within the analytical framework developed here.

Finally, we note that the analysis of the theoretical model developed in this paper has focused on situations where the initial shape is conic or formed by two intersecting planes. These cases result in special $t^{4/5}$ similarity solutions for all time. For more general bodies, a rich variety of regime transitions in the temporal exponents of tip descent rates, occur. This includes the case of initially rectangular bodies, as is representative of the initial shape of ice bergs or ice cubes. These broader themes, including the determination of the intrinsic scales of melting or dissolution of such bodies, will form the focus of our companion paper (Pegler & Davies Wykes 2020).

The authors thank the directors of the Woods Hole Oceanographic Institute Geophysical Fluid Dynamics Program in 2019 for supporting us as staff members during this work. We are grateful to Dr Claudia Cenedese for use the Geophysical Fluid Dynamics Laboratory to conduct our experiments, to Anders Jensen for helping to set them up, and to Ann Newbury for use of her kitchen to prepare the candy samples.

Appendix A. Latent heating

As a solid dissolves, chemical energy is transferred to heat energy (or vice versa) as a consequence of the new chemical arrangement produced by solvation. The result is an exothermic or endothermic reaction that can produce latent heating or cooling. In principle, this heating can affect the dynamics by changing the saturation concentration C_{sat} , buoyancy force and/or viscosity. To check the significance of these effects, we derive a formula for the maximal temperature change arising from the dissolution. To this end, we introduce the energy equation for the evolution of temperature,

$$u \frac{\partial T}{\partial s} + v \frac{\partial T}{\partial y} = \frac{\partial}{\partial y} \left(\kappa_T \frac{\partial T}{\partial y} \right), \quad (\text{A } 1)$$

where κ_T is the thermal diffusivity. To model the latent heating, we apply the condition

$$-\kappa_T \frac{\partial T}{\partial y} = \frac{Q}{c_p \rho_l} = \Lambda \left(-\kappa \frac{\partial C}{\partial y} \right) \quad (y = 0), \quad (\text{A } 2)$$

where Q is the flux of heat per unit area produced through latent heating, c_p is the specific heat capacity of the fluid, ρ_l is the density of the fluid, and Λ is a conversion factor between temperature flux and concentration flux. In writing the condition above, we have assumed that all the latent heat is inputted into the fluid, which is consistent with assuming that the heat has spread and equilibrated laterally through the solid. To derive the second equality in (A 2) and evaluate Λ , we note first that the heat released per unit volume of dissolved solid can be evaluated as $H\rho_s/M$, where H (J/mol) is the energy released per unit mol of sugar dissolved, M (g/mol) is the molar mass of sugar, and ρ_s is the density of solid sugar. The dissolving surface recedes at the speed V and hence the heat flux per unit area of the interface is $Q = VH\rho_s/M$. Combining this equation with (2.4) and (A 2), we obtain $\Lambda \equiv H/Mc_p(C_i - C_s)$. For the values corresponding to sucrose and water, $H \approx 16.9$ kJ/mol (Mathlouthi & Reiser 2012), $M \approx 342$ g/mol, and $c_p \approx 4.18$ J/gK (Haynes 2016), we evaluate the conversion parameter to be $\Lambda \approx 36$ K.

As a check on the self-consistency of assuming that latent heating is negligible, we derive here an approximation for the wall temperature increase under the assumption that the flow rate is represented by the streamfunction $F(\eta)$ predicted by the solutal system of (C 5)–(C 6). Let $T = (C_i\Lambda)\vartheta$ define a dimensionless temperature ϑ . Recasting (A 1) and (A 2) in terms of (C 4), we obtain

$$-F\vartheta' = \varepsilon^{-1}\vartheta'', \quad \vartheta'(0) = \varepsilon\phi'(0), \quad (\text{A } 3a,b)$$

where $\varepsilon \equiv \kappa/\kappa_T$ is the inverse of the Lewis number. Values ranging from $\varepsilon \approx 10^{-4}$ to 10^{-3} apply to sugar solutions at room temperature (Mohos 2010; Haynes 2016).

For $\varepsilon \rightarrow 0$, the solutal layer is considerably smaller than the thermal layer. Thus, we assume that the thermal advection is driven to good approximation by the far-field of the solutal layer governed by (C 5)–(C 6). Let $F \sim F_0 + U\eta$ denote the far-field streamfunction predicted by these equations. For $B = 0$ and constant μ and κ , $F_0 \approx -0.730$ and $U \approx 1.021$, for example. The solution to (A 3a) subject to (A 3b) and $\vartheta(\infty) = 0$ can then be determined in the form

$$\vartheta = -\phi'(0) \sqrt{\frac{\pi\varepsilon}{2U}} \exp\left(\frac{F_0^2\varepsilon}{2U}\right) \operatorname{erfc}\left[\sqrt{\frac{U\varepsilon}{2}}\left(\eta + \frac{F_0}{U}\right)\right]. \quad (\text{A } 4)$$

Evaluating this expression at the wall, $\eta = 0$, retaining only leading-order terms in the limit $\varepsilon \rightarrow 0$, and reverting to the dimensional temperature, we obtain the prediction for the increase in the wall temperature due to latent heating as

$$T_s = \Omega\sqrt{\varepsilon}C_s\Lambda, \quad (\text{A } 5)$$

where $\Omega \equiv -\phi'(0)\sqrt{\pi/2U}$ is a dimensionless prefactor determined from the solution to (C 5)–(C 6). For example, $\Omega = 0.62$ for the case of constant fluid properties and $B = 0$. Using values of κ for candy solution ranging from a dilute to a fully saturated solution, the increase in wall temperature relative to the far field is predicted to be at most $T_s \approx 0.8$ K. This increase has a negligible effect on the saturation concentration C_{sat} (the change is approximately 0.2%), confirming that the assumption of constant C_i in (2.2) is reasonable. The density change of water due to thermal expansion from 20 to 20.8 °C is less than 0.1% of the density change between water and saturated sucrose solution, indicating that concentration differences provide the dominant control of buoyancy.

Appendix B. Gradient versus slope control in free convection

This appendix presents a general model of a solutal (or thermal) boundary layer that can account simultaneously for the along-slope component of buoyancy and horizontal gradients in hydrostatic pressure. The model thus allows for intermediate situations arising on mild slopes for which these contributions can both be significant. We use the model to derive an intrinsic length scale on which a transition between the contributions occurs. To this end, we write down the generalised boundary-layer system

$$\frac{\partial u}{\partial s} + \frac{\partial v}{\partial y} = 0 \quad (\text{B1})$$

$$\rho \left(u \frac{\partial u}{\partial s} + v \frac{\partial u}{\partial y} \right) = -\frac{\partial p}{\partial s} + \frac{\partial}{\partial y} \left(\mu \frac{\partial u}{\partial y} \right) + \rho g \sin \alpha \quad (\text{B2})$$

$$\frac{\partial p}{\partial y} = -\rho g \cos \alpha \quad (\text{B3})$$

$$u \frac{\partial C}{\partial s} + v \frac{\partial C}{\partial y} = \frac{\partial}{\partial y} \left(\kappa \frac{\partial C}{\partial y} \right), \quad (\text{B4})$$

where p is pressure, which retains the pressure gradient and gravitational forces in (B2), as appear in the full Navier-Stokes equations (Stewartson 1958). The model above requires the same assumptions of quasi-steadiness and sufficiently low curvature as underlies the model of (2.9)–(2.11). Using (2.1) to substitute ρ in favour for the concentration field C in (B3) and then integrating this equation with respect to a reference far-field background pressure $p = p_0$ at level $z = z_0$, we obtain the hydrostatic pressure

$$p = p_0 - \rho_0 g [y - y_0(s)] \cos \alpha - \Delta \rho_s g \cos \alpha \int_{y_0(s)}^y C(s, \tilde{y}) \, d\tilde{y}, \quad (\text{B5})$$

where $y_0(s) \equiv z_0 / \sin \alpha$. Since we are only concerned here with the boundary-layer dynamics, we notationally omit the t dependences of variables in this appendix. On using (2.1) to substitute for ρ in (B2) and using (B5) to substitute for p we obtain, on simplification, the generalised momentum equation

$$\rho \left(u \frac{\partial u}{\partial s} + v \frac{\partial u}{\partial y} \right) = \frac{\partial}{\partial y} \left(\mu \frac{\partial u}{\partial y} \right) + \Delta \rho_s g \left[(\sin \alpha) C + \cos \alpha \frac{\partial}{\partial s} \int_{y_0(s)}^y C(s, \tilde{y}) \, d\tilde{y} \right], \quad (\text{B6})$$

where we have cancelled the terms depending on the background density ρ_0 and neglected terms of order $\alpha_s y \ll 1$ under the thin-flow assumption. Equation (B6) contains a new term compared to (2.10) representing the gradient in weight of fluid columns above any given position. Flows driven independently by this gradient have been considered previously in the context of horizontal thermal boundary layers (e.g. Stewartson 1958; Neufeld *et al.* 2010) and stratified gravity currents (Pegler *et al.* 2016).

For non-horizontal substrates, we anticipate the gradient terms to drive the flow in a region near the top of the dissolving or heated wall (i.e. the tip of a dissolving body), and transition to a region dominated by the along-slope term sufficiently far downstream. The first of these regions, referred to as the *gradient-driven region*, will arise first because the concentration gradients are relatively large near the origin of the boundary layer, whilst the along-slope component of gravity is zero. As the aspect ratio of the boundary layer becomes more slender, along-flow gradients will reduce and the along-slope contribution to buoyancy will begin to dominate, forming the *slope-driven region* (see figure 15).

A scaling relationship formed from the two terms comprising the buoyancy force in (B6) indicates that these two contributions are comparable if $y \sim x h_x$. The scaling

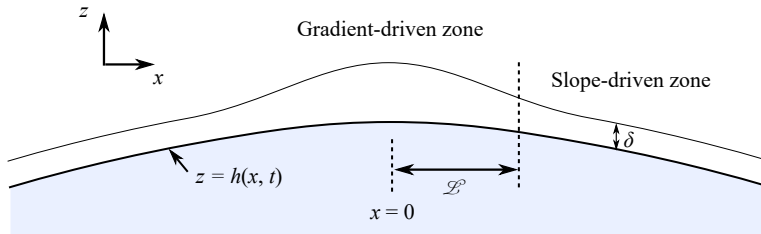


FIGURE 15. Schematic illustrating the transition between the gradient-driven zone and the slope-driven zone of a free-convective boundary layer over the length scale \mathcal{L} derived in appendix B, shown for an illustrative parabolic surface ($n = 2$).

between the viscous and buoyancy forces in (B 6) yields $\mu u \sim \Delta \rho g C_i h_x y^2$. The further balance between advection and diffusion in (B 4) yields $u \sim \kappa x / y^2$. Eliminating u from these last two scalings, we obtain

$$\mu \kappa x \sim \Delta \rho g h_x C_i y^4. \quad (\text{B } 7)$$

Using the scaling of $y \sim x h_x$ to eliminate y in (B 7), we obtain

$$h_x^5 x^3 \sim \frac{\nu \kappa}{C_i g'} \equiv \mathcal{L}_*^3, \quad (\text{B } 8)$$

where $g' \equiv (\Delta \rho_s / \rho) g$ and $\nu \equiv \mu / \rho$. We note in passing that $\mathcal{L}_* \equiv (\nu \kappa / C_i g')^{1/3}$ is the unique intrinsic horizontal length scale arising in Rayleigh-Bénard convection giving, up to a dimensionless prefactor, the wavelength on which convective fingers form at a heated or cooled boundary (Bejan 2013). It has arisen here because the set of scalings involving viscous, advective, diffusive and buoyant terms is equivalent. However, a new factor of h_x has emerged here owing to the slope dependence of the buoyancy force.

To allow for a range of surface slopes, we let $h = -c_n x^n$, where c_n and n are constants. Substituting the implied scaling $h_x \sim c_n x^{n-1}$ in (B 8) and rearranging, we obtain

$$x \sim (\mathcal{L}_*^3 c_n^{-5})^{\frac{1}{5n-2}} \equiv \mathcal{L}, \quad (\text{B } 9)$$

providing the unique intrinsic length scale emerging from scaling to characterise the transition between a gradient-driven region and a slope-driven region. The case of (B 9) for $n = 1$ has been derived by Stewartson (1958). For sharp concave shapes with $n < 2/5$, we anticipate that the transition between along-slope control and gradient control is reversed, with a similarity solution applying for all time if $n = 2/5$ (a mathematically analogous switch arises for gravity currents on topography; Pegler *et al.* 2013).

Appendix C. Dissolution profiles for arbitrary two-dimensional bodies under stable free convection

This appendix develops the expression (2.15) describing the dissolution pattern due to steady natural-convective two-dimensional boundary layer of arbitrary shape at high Schmidt number. The result has been derived previously by Acrivos (1960a). The review here is conducted in particular to emphasise the generality of the result in applying for fluids of general dependences of density, viscosity and diffusivity on concentration, and to illustrate how these dependences become encapsulated within a single parameter, referred to as A . Let us define dimensionless forms of the functions relating viscosity and diffusivity to concentration by

$$\mu = \mu_\infty \hat{\mu}(\phi), \quad \kappa = \kappa_\infty \hat{\kappa}(\phi), \quad (\text{C } 1)$$

where μ_∞ and κ_∞ are the viscosity and diffusivity of the solvent in its pure form (so that $\hat{\mu}(0) = 1$ and $\hat{\kappa}(0) = 1$ without loss of generality), and $\phi \equiv C/C_i$ is a normalised concentration. The inertialess momentum equation (2.10) can then be written

$$0 = \frac{\partial}{\partial y} \left(\hat{\mu}(\phi) \frac{\partial u}{\partial y} \right) + \left(\frac{\Delta \rho_s g C_i}{\mu_\infty} \right) \sin[\alpha(s)] \phi, \quad (\text{C } 2)$$

We have here notationally omitted t arguments, as we are concerned here only with the quasi-steady boundary-layer system. In a high- Sc boundary layer, the flow separates into an inner low- Re region, in which a balance between viscous stresses and buoyancy applies in accordance with (C 2), and a much larger outer region, in which the velocity decays to zero to satisfy (2.13) under a balance between viscous and inertial forces. In this situation, one can focus on the analysis of the inner region and apply the matching no-stress condition (Morgan & Warner 1956; Acrivos 1960*a,b*, 1962; Kuiken 1968),

$$\frac{\partial u}{\partial y} \rightarrow 0, \quad \text{as } y \rightarrow \infty. \quad (\text{C } 3)$$

The condition of far-field stagnancy (2.13*b*) is not imposed on the inertialess inner region, which is instead satisfied by the inertio-viscous outer region.

Since the flow is incompressible, we introduce the streamfunction $\psi(s, y)$ defined such that $u = \psi_y$ and $v = -\psi_s$. Let us transform the system given by (2.9), (2.11) and (C 2) in terms of the new variables (Acrivos 1960*a*)

$$\eta = G(s)^{1/3} \left(\int_0^s G(s)^{1/3} ds \right)^{-\frac{1}{4}} y, \quad F(\eta) = \frac{1}{\kappa_\infty} \left(\int_0^s G(s)^{1/3} ds \right)^{-\frac{3}{4}} \psi, \quad (\text{C } 4a,b)$$

where $G(s) \equiv G_* \sin[\alpha(s)]$ and $G_* \equiv \Delta \rho_s g C_i / \kappa_\infty \mu_\infty$. The momentum equation (C 2) and solute transport equation (2.11) become (using primes to denote $d/d\eta$)

$$0 = [\hat{\mu}(\phi) F'''] + \phi, \quad -F\phi' = [\hat{\kappa}(\phi)\phi']', \quad (\text{C } 5a,b)$$

respectively. Conditions (2.2), (2.12*a,b*) and (2.13*a*) and (C 3) become

$$\phi(0) = 1, \quad F(0) = B\phi'(0), \quad F'(0) = 0, \quad \phi(\infty) = 0, \quad F''(\infty) = 0. \quad (\text{C } 6)$$

where $B = (4/3)(\kappa_i/\kappa_\infty)C_i/(1 - C_i)$ is a dimensionless parameter. The transformation has rendered the boundary-layer system entirely free of $h(x)$. The reduced system is equivalent to the similarity equations describing free convection along a vertical wall (Ostrach 1953). By recasting the dimensionless solution to (C 5)–(C 6) back in terms of the original variables, we develop expressions for properties of natural-convective boundary layers that apply for arbitrary shape profiles $h(x)$. In terms of the transformed variables, the pattern of the dissolution rate along the boundary (2.3) can be determined as

$$q = -\kappa_i \frac{\partial C}{\partial y} = \frac{\gamma \kappa_i C_i G(s)^{1/3}}{[\int_0^s G(s)^{1/3} ds]^{1/4}} = \frac{D(\sin \alpha)^{1/3}}{[\int_0^s (\sin \alpha)^{1/3} ds]^{1/4}}, \quad (\text{C } 7)$$

where $D = \gamma \kappa_i C_i G_*^{1/4}$ and $\gamma \equiv -\phi'(0)$ is the dimensionless flux of solute mass, determined by solving (C 5)–(C 6). For example, $\gamma \approx 0.5027$ for the case of constant properties, $\hat{\mu} \equiv \hat{\kappa} \equiv 1$, and $B \approx 0$ (obtained using a shooting method in which $\phi(0)$, $F(0)$ and $F'(0)$ are imposed using (C 7), and $\phi'(0)$ and $F''(0)$ are treated as shooting parameters). On using (C 7) to evaluate q in (2.3), we obtain the required result of (2.15).

C.1. Scalings for velocity, interface flux and boundary-layer thickness

Here, we develop expressions for the velocity and thickness of the boundary-layer flow, which are used in sections 2.2 and 2.3. By combining (C4a, b), one determines the longitudinal velocity field as

$$u = \frac{\partial \psi}{\partial y} = \kappa_\infty G^{1/3} \left(\int_0^s G(s)^{1/3} ds \right)^{\frac{1}{2}} \psi'(\eta) \quad (\text{C8})$$

For a shallow body ($\alpha \ll 1$), the arc length can be approximated by the horizontal coordinate, $s \approx x$. For the case of a shallow body described by a power-law height profile $h = -cx^n$, (C8), (C7) and (C4a) yield the scalings for the velocity, solutal flux and boundary-layer thickness,

$$u \sim \kappa_\infty (cG_* x^n)^{1/2}, \quad q \sim Dc^{1/4} x^{(n-2)/4}, \quad \delta \sim (cG_* x^{-(n-2)})^{1/4}, \quad (\text{C9})$$

respectively. For a general steep body ($\alpha \approx \pi/2$), the corresponding results are

$$u \sim \kappa_\infty (-G_* z)^{1/2}, \quad q \sim D(-z)^{1/4}, \quad \delta \sim G_*^{-1/4} (-z)^{1/4}. \quad (\text{C10})$$

Appendix D. Numerical scheme for solving the full model

We solved (2.16) numerically using an explicit second-order upwind finite-difference scheme. It should be noted that ‘upwind’ refers here to the characteristics of the evolution equation (2.16), as opposed to the flow itself. To determine the direction of propagation of the characteristics, we write (2.16) in the canonical form

$$\left(\frac{\partial}{\partial t} + u_c \frac{\partial}{\partial x} \right) h = 0, \quad \text{where} \quad u_c \equiv - \frac{\partial h}{\partial t} / \frac{\partial h}{\partial x} \quad (\text{D1a,b})$$

is the velocity of the characteristics. Since $\partial h / \partial t < 0$ in accordance with (2.16), it follows that $\text{sgn}(u_c) = \text{sgn}(h_x) < 0$. Thus, the characteristics propagate in the negative x direction, which is indeed against the flow. This can be understood by noting that dissolution causes the shape to recede *inwards*, i.e. the negative x -direction.

Let H denote the initial height of the body, with $z = -H$ denoting the rigid surface on which it rests. Let $x_B(t)$ denote the horizontal position of the base of the dissolving body, where the vertical extent of the body vanishes,

$$h(x_B(t), t) = -H. \quad (\text{D2})$$

Like the tip of the body, the horizontal extent of the base $x_B(t)$ will also evolve. Differentiating (D2) with respect to time, we obtain the evolution equation for the base of the body

$$\dot{x}_B = - \frac{\partial h}{\partial t} / \frac{\partial h}{\partial x} \quad \text{at } x = x_B(t), \quad (\text{D3})$$

where the numerator can be determined using (2.16). One approach to model the evolution of the base of the body numerically would be to recast the system in terms of the new spatial coordinate $X = x/x_B(t)$, and evolve the basal front according to (D3). In this method, the numerical domain would correspond precisely to the domain of the body. Alternatively, one can work with a fixed domain, and simply treat the thickness exterior to the base of the body as zero, so $h = -H$ for $x > x_B(t)$. For this, we let x_i denote a fixed, equally-spaced spatial grid of nodes, where $1 \leq i \leq N$, with $x_1 = 0$. Let t_n denote the set of temporal nodes. Let $h_i^n \equiv h(x_i, t_n)$. Within this interpretation,

$x_B(t)$ can be defined numerically as the first node, denoted $i = B$, at which the vertical depth of the body, $(H + h)$, is first non-zero as one moves leftwards from the rightmost node. Numerically, the thickness of the body to the right of this node can simply be treated as equal to zero ($h = -H$). According to (2.16), $\partial h/\partial t = 0$ if $\partial h/\partial x = 0$ and hence the numerical representation of the height variable in the region $x_B(t) < x < x_N$ remains uniformly fixed at zero vertical thickness ($h = -H$). Indeed, this is analogous to how viscous gravity currents (and similar free-boundary problems) can be represented numerically on a fixed grid of nodes. Likewise, the domain is separated between a region containing the current and a region of zero thickness downstream of the nose. In the present context of our dissolving body, an alternative physical interpretation is that the region $x > x_B(t)$ forms a horizontal surface $z = -H$ of the same material comprising the dissolving body, and the region $x < x_B(t)$ forms a localised protrusion from this otherwise horizontal surface.

Due to its ease, we apply the method of a fixed numerical domain described above. We choose the spatial domain $[0, x_N]$ to be at least as large as is necessary to fit our initial shape, and discretise the time derivative in (2.16) using forwards Euler,

$$\frac{\partial h}{\partial t} = \begin{cases} \frac{h_i^{n+1} - h_i^n}{\delta t} + O(\delta t) & (1 \leq i \leq N - 1), \\ 0 & (i = N). \end{cases} \quad (\text{D } 4)$$

The rate of change of the final node is here specified as zero, so as to ensure that the vertical thickness of the body outside its base is prescribed numerically as zero, as discussed above. As an aside, we note that, since we are only interested in the model prediction within the domain of the body, $x < x_B(t)$, in fact *any* non-positive prescription of $\partial h/\partial t$ at the final numerical node $i = N$ results in the same prediction inside the body $x < x_B(t)$ where $h > -H$. This independence applies because once the surface descends below any given height level, it no longer influences the evolution of the shape above that level. The spatial derivatives were approximated using a second-order upwind scheme,

$$\frac{\partial h}{\partial x} = \begin{cases} \frac{-3h_i^n + 4h_{i+1}^n - h_{i+2}^n}{2\delta x} + O(\delta x^2). & (1 \leq i \leq N - 2) \\ \frac{-h_i^n + h_{i+1}^n}{\delta x} + O(\delta x) & (i = N - 1) \end{cases} \quad (\text{D } 5)$$

As specified here, a first-order discretisation was used for node $i = N - 1$ only. No spatial discretisation was necessary at $i = N$, where h remains fixed in accordance with (D 4). Second-order spatial discretisation was found to be required in order to yield good accuracy to long times. Having approximated $\partial h/\partial x$ using (D 5), the integral in (2.16) was evaluated using Simpson's rule. The accuracy and convergence of the solver was verified by comparison with the similarity solutions calculated in section 3, showing convergence with spatial and temporal resolution. For our computations, we used $N \geq 1000$ and $\delta t < 10^{-4}$.

Appendix E. Analytical solution for the steep similarity solution

This appendix derives the analytical solution to (3.18) given by (3.19). First, we apply a transformation that switches the dependent and independent variable, defined by $\zeta = \phi(\eta)$, and $X(\zeta) = \eta$. The transformed form of (3.18) is

$$\frac{4}{5}(\zeta X' - X) = (\phi_0 - \zeta)^{-1/4} \quad (\text{E } 1)$$

Multiplying by the integrating factor ζ^{-2} and forming the exact differential, we obtain

$$\frac{4}{5} (\zeta^{-1} X)' = \frac{\zeta^{-2}}{(\phi_0 - \zeta)^{1/4}}. \quad (\text{E } 2)$$

On integration subject to the condition $X(\phi_0) = 0$, we obtain

$$\frac{4}{5} X = \zeta \int_{\phi_0}^{\zeta} \frac{\zeta^{-2}}{(\phi_0 - \zeta)^{1/4}} d\zeta. \quad (\text{E } 3)$$

Changing the integration variable to $\chi = \zeta/\phi_0$ and reverting to the variables (η, ϕ) , we obtain (3.19).

Appendix F. Dissolution profiles for axisymmetric bodies

This appendix reviews the development of the expression for the dissolution pattern created by natural convection along the exterior of an axisymmetric body of arbitrary shape (4.4) derived previously by Acrivos (1960*b*). Owing to the presence of r in (4.1), it should be noted that the transform applied in the two-dimensional case in appendix C (Acrivos 1960*a*) fails to eliminate $h(r, t)$ from the system, at least directly. However, we can first apply a transformation of the axisymmetric boundary-layer equations that renders them equivalent in mathematical form to the two-dimensional equations (2.9)–(2.11) (Mangler 1948; Acrivos 1960*b*).

Let (s, y, u, v, C) denote the axisymmetric variables used in (4.1)–(4.3). Let

$$\tilde{s} = \int_0^s r^2 ds, \quad \tilde{y} = ry, \quad \tilde{u} = u, \quad \tilde{v} = \frac{1}{r} \left(v + \frac{yu}{rs_r} \right), \quad \tilde{C} = C. \quad (\text{F } 1)$$

In terms of these new variables, (4.1)–(4.3) transform to

$$\frac{\partial \tilde{u}}{\partial \tilde{s}} + \frac{\partial \tilde{v}}{\partial \tilde{y}} = 0, \quad (\text{F } 2)$$

$$\rho \left(\tilde{u} \frac{\partial \tilde{u}}{\partial \tilde{s}} + \tilde{v} \frac{\partial \tilde{u}}{\partial \tilde{y}} \right) = \frac{\partial}{\partial \tilde{y}} \left(\mu \frac{\partial \tilde{u}}{\partial \tilde{y}} \right) + \frac{\Delta \rho g \sin[\alpha(s, t)]}{r^2} \tilde{C}, \quad (\text{F } 3)$$

$$\tilde{u} \frac{\partial \tilde{C}}{\partial \tilde{s}} + \tilde{v} \frac{\partial \tilde{C}}{\partial \tilde{y}} = \frac{\partial}{\partial \tilde{y}} \left(\kappa \frac{\partial \tilde{C}}{\partial \tilde{y}} \right). \quad (\text{F } 4)$$

These equations are identical to (2.9)–(2.11) except with $\sin \alpha$ replaced by $r^{-2} \sin \alpha$. Applying the result of appendix C to (4.1)–(4.3) with the r^{-2} included, we obtain

$$-\kappa_s \frac{\partial \tilde{C}}{\partial \tilde{y}} = \frac{D(r^{-2} \sin \alpha)^{1/3}}{[\int_0^s (r^{-2} \sin \alpha)^{1/3} d\tilde{s}]^{1/4}}, \quad (\text{F } 5)$$

where the coefficient D is defined following (C 7). Recasting (F 5) in terms of the original variables, with use of $d\tilde{s} = r^2 ds$ to transform the integration variable, the mass flux along the boundary is determined as (Acrivos 1960*b*)

$$q = -\kappa_s \frac{\partial C}{\partial y} = r \left(-\kappa_s \frac{\partial \tilde{C}}{\partial \tilde{y}} \right) = \frac{D(r \sin \alpha)^{1/3}}{[\int_0^s (r^4 \sin \alpha)^{1/3} ds]^{1/4}}. \quad (\text{F } 6)$$

yielding the required relationship (4.4).

REFERENCES

- ACRIVOS, A. 1960a Mass transfer in laminar boundary-layer flows with finite interfacial velocities. *AIChE Journal* **6** (3), 410–414.
- ACRIVOS, A. 1960b A theoretical analysis of laminar natural convection heat transfer to non-Newtonian fluids. *AIChE Journal* **6** (4), 584–590.
- ACRIVOS, A. 1962 The asymptotic form of the laminar boundary-layer mass-transfer rate for large interfacial velocities. *Journal of Fluid Mechanics* **12** (3), 337357.
- BEJAN, A. 2013 *Convection Heat Transfer*, 4th edn. John Wiley & Sons, Ltd.
- CAMPOREALE, C. & RIDOLFI, L. 2012 Hydrodynamic-Driven Stability Analysis of Morphological Patterns on Stalactites and Implications for Cave Paleoflow Reconstructions. *Physical Review Letters* **108** (23).
- CAREY, V. P. & GEBHART, B. 1982 Transport near a vertical ice surface melting in saline water: experiments at low salinities. *Journal of Fluid Mechanics* **117**, 403–423, publisher: Cambridge University Press.
- CAREY, V. P., GEBHART, B. & MOLLENDORF, J. C. 1980 Buoyancy force reversals in vertical natural convection flows in cold water. *Journal of Fluid Mechanics* **97** (2), 279–297, publisher: Cambridge University Press.
- DALLASTON, M. C., HEWITT, I. J. & WELLS, A. J. 2015 Channelization of plumes beneath ice shelves. *Journal of Fluid Mechanics* **785**, 109–134.
- DAVIES WYKES, M. S., HUANG, J. M., HAJJAR, G. A. & RISTROPH, L. 2018 Self-sculpting of a dissolvable body due to gravitational convection. *Physical Review Fluids* **3** (4).
- DUTRIEUX, P., STEWART, C., JENKINS, A., NICHOLLS, K. W., CORR, H. F. J., RIGNOT, E. & STEFFEN, K. 2014 Basal terraces on melting ice shelves. *Geophysical Research Letters* **41** (15), 5506–5513.
- EPSTEIN, M. & CHEUNG, F. B. 1983 Complex Freezing-Melting Interfaces in Fluid Flow. *Annual Review of Fluid Mechanics* **15** (1), 293–319.
- FITZMAURICE, A., CENEDESE, C. & STRANEO, F. 2017 Nonlinear response of iceberg side melting to ocean currents. *Geophysical Research Letters* **44** (11), 5637–5644, eprint: <https://agupubs.onlinelibrary.wiley.com/doi/pdf/10.1002/2017GL073585>.
- HAO, Y. L. & TAO, Y.-X. 2001 Melting of a Solid Sphere Under Forced and Mixed Convection: Flow Characteristics. *Journal of Heat Transfer* **123** (5), 937.
- HAO, Y. L. & TAO, Y.-X. 2002 Heat Transfer Characteristics of Melting Ice Spheres Under Forced and Mixed Convection. *Journal of Heat Transfer* **124** (5), 891.
- HAYNES, W. M. 2016 *CRC Handbook of Chemistry and Physics*, 97th edn. CRC Press.
- HEWITT, I. J. 2020 Subglacial Plumes. *Annual Review of Fluid Mechanics* **52** (1).
- HUANG, J. M., MOORE, M. N. J. & RISTROPH, L. 2015 Shape dynamics and scaling laws for a body dissolving in fluid flow. *Journal of Fluid Mechanics* **765**.
- HUPPERT, H. E. & TURNER, J. S. 1978 On melting icebergs. *Nature* **271** (5640), 46–48.
- HUPPERT, H. E. & TURNER, J. S. 1980 Ice blocks melting into a salinity gradient. *Journal of Fluid Mechanics* **100** (2), 367–384.
- IVANTSOV, G. P. 1985 Temperature field around a spherical, cylindrical, and needle-shaped crystal, growing in a pre-cooled melt .
- JAEGER, J. C. & CARSLAW, H. S. 1959 *Conduction of heat in solids*. Clarendon Press.
- JOSBERGER, E. G. & MARTIN, S. 1981 A laboratory and theoretical study of the boundary layer adjacent to a vertical melting ice wall in salt water. *Journal of Fluid Mechanics* **111** (-1), 439.
- KERR, R. C. 1994 Dissolving driven by vigorous compositional convection. *Journal of Fluid Mechanics* **280**, 287–302.
- KERR, R. C. & MCCONNOCHIE, C. D. 2015 Dissolution of a vertical solid surface by turbulent compositional convection. *Journal of Fluid Mechanics* **765**, 211–228.
- KUIKEN, H. K. 1968 An asymptotic solution for large Prandtl number free convection. *Journal of Engineering Mathematics* **2** (4), 355–371.
- MAKKONEN, L. 1988 A model of icicle growth. *Journal of Glaciology* **34** (116), 64–70.
- MANGLER, W. 1948 Zusammenhang zwischen ebenen und rotationssymmetrischen grenzschichten in kompressiblen flüssigkeiten. *ZAMM* **28** (4), 97–103.

- MATHLOUTHI, M. & REISER, P. 2012 *Sucrose: Properties and Applications*. Springer Science & Business Media, google-Books-ID: 0VzmBwAAQBAJ.
- MC CONNOCHIE, C. D. & KERR, R. C. 2018 Dissolution of a sloping solid surface by turbulent compositional convection. *Journal of Fluid Mechanics* **846**, 563–577.
- MCLEOD, P., RILEY, D. S. & SPARKS, R. S. J. 1996 Melting of a sphere in hot fluid. *Journal of Fluid Mechanics* **327**, 393–409.
- MCPHEE, M. 2008 *Air-Ice-Ocean Interaction*. Springer.
- MEAKIN, P. & JAMTVEIT, B. 2010 Geological pattern formation by growth and dissolution in aqueous systems. *Proceedings of the Royal Society A: Mathematical, Physical and Engineering Sciences* **466** (2115), 659–694.
- MERK, H. J. & PRINS, J. A. 1953 Thermal convection in laminary boundary layers. I. *Applied Scientific Research, Section A* **4** (1), 11–24.
- MOHOS, F. Á. 2010 *Confectionery and chocolate engineering: principles and applications*. Blackwell Pub.
- MOORE, M. N. J. 2017 Riemann-Hilbert Problems for the Shapes Formed by Bodies Dissolving, Melting, and Eroding in Fluid Flows. *Communications on Pure and Applied Mathematics* **70** (9), 1810–1831.
- MOORE, M. N. J., RISTROPH, L., CHILDRESS, S., ZHANG, J. & SHELLEY, M. J. 2013 Self-similar evolution of a body eroding in a fluid flow. *Physics of Fluids* **25** (11), 116602.
- MORGAN, G. W. & WARNER, W. H. 1956 On heat transfer in laminar boundary layers at high Prandtl number. *Journal of the Aeronautical Sciences* **23** (10), 937–948.
- NAKOUZI, E., GOLDSTEIN, R. E. & STEINBOCK, O. 2015 Do Dissolving Objects Converge to a Universal Shape? *Langmuir* **31** (14), 4145–4150.
- NASH, G. E. & GLICKSMAN, M. E. 1979 Steady-State Dendritic Growth. In *Growth of Crystals: Volume 11* (ed. A. A Chernov), pp. 284–289. Boston, MA: Springer US.
- NEUFELD, J. A., GOLDSTEIN, R. E. & WORSTER, M. G. 2010 On the mechanisms of icicle evolution. *Journal of Fluid Mechanics* **647**, 287.
- OSTRACH, S. 1953 An analysis of laminar free-convection flow and heat transfer about a flat plate parallel to the direction of the generating body force. *Tech. Rep.* 1111. NASA.
- PEGLER, S. S. & DAVIES WYKES, M. S. 2020 Regimes of melting and dissolving bodies under natural convection. *Journal of Fluid Mechanics* Companion paper.
- PEGLER, S. S., HUPPERT, H. E. & NEUFELD, J. A. 2016 Stratified gravity currents in porous media. *Journal of Fluid Mechanics* **791**, 329–357.
- PRICE, H. C., MATTSSON, J. & MURRAY, B. J. 2016 Sucrose diffusion in aqueous solution. *Physical Chemistry Chemical Physics* **18** (28), 19207–19216.
- QUINTAS, M., BRANDO, T., SILVA, C. & CUNHA, R. 2006 Rheology of supersaturated sucrose solutions. *Journal of Food Engineering* **77** (4), 844–852.
- RISTROPH, L. 2018 Sculpting with flow. *Journal of Fluid Mechanics* **838**, 1–4.
- RISTROPH, L., MOORE, M. N. J., CHILDRESS, S., SHELLEY, M. J. & ZHANG, J. 2012 Sculpting of an erodible body by flowing water. *Proceedings of the National Academy of Sciences* **109** (48), 19606–19609.
- SCHLICHTING, H. & GERSTEN, K. 2017 *Boundary-Layer Theory*, 9th edn. Springer-Verlag Berlin Heidelberg.
- SHORT, M. B., BAYGENTS, J. C. & GOLDSTEIN, R. E. 2006 A free-boundary theory for the shape of the ideal dripping icicle. *Physics of Fluids* **18** (8), 083101.
- SLATER, D. A., NIENOW, P. W., GOLDBERG, D. N., COWTON, T. R. & SOLE, A. J. 2017 A model for tidewater glacier undercutting by submarine melting. *Geophysical Research Letters* **44** (5), 2360–2368.
- STEFAN, J. 1891 Ueber die theorie der eisbildung, insbesondere ber die eisbildung im polarmeere. *Annalen der Physik* **278** (2), 269–286.
- STEWARTSON, K. 1958 On the free convection from a horizontal plate. *ZAMP* **9** (3), 276–282.
- SULLIVAN, T. S., LIU, Y. & ECKE, R. E. 1996 Turbulent solutal convection and surface patterning in solid dissolution. *Physical Review E* **54** (1), 486–495.
- VANIER, C. R. & TIEN, C. 1970 Free convection melting of ice spheres. *AIChE Journal* **16** (1), 76–82.

WELLS, A. J. & WORSTER, M. G. 2011 Melting and dissolving of a vertical solid surface with laminar compositional convection. *Journal of Fluid Mechanics* **687**, 118–140.